






Development of synaptic fidelity and action potential robustness at an inhibitory sound localization circuit: effects of otoferlin-related deafness

Nicolas I.C. Müller^{1,2} , Isabelle Paulußen¹ , Lina N. Hofmann¹, Jonas O. Fisch¹ , Abhyudai Singh³  and Eckhard Friauf¹ 

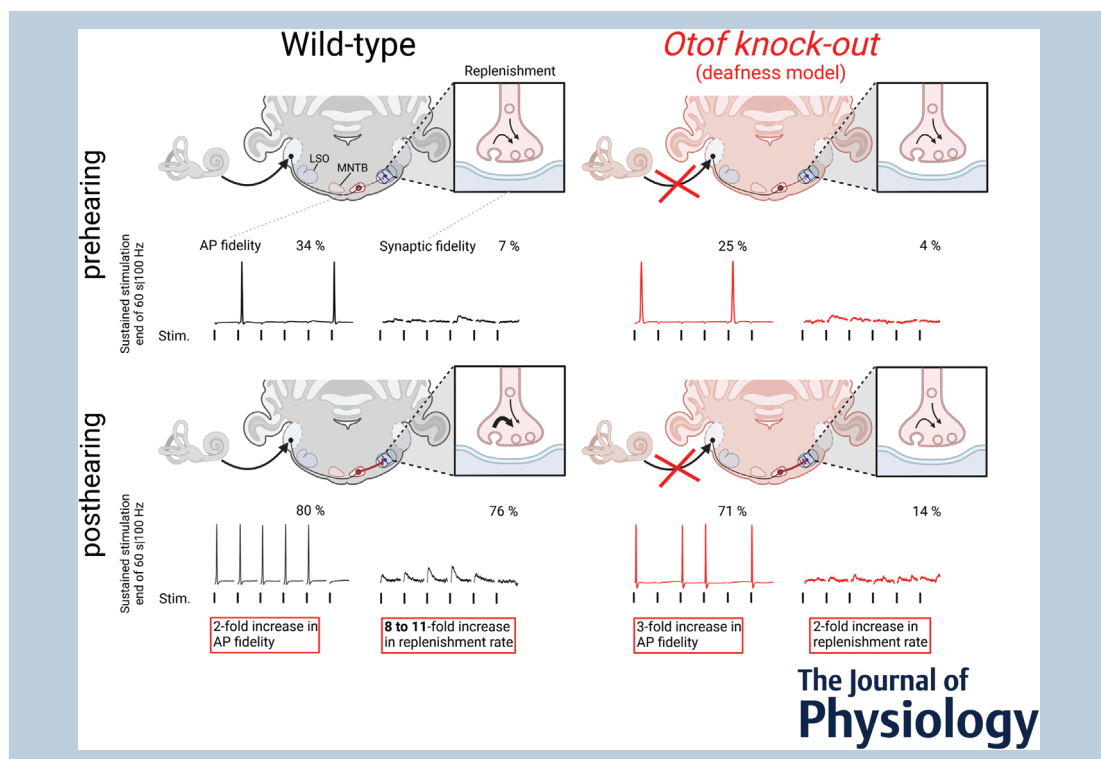
¹Animal Physiology Group, Department of Biology, University of Kaiserslautern, Kaiserslautern, Germany

²Physiology of Neuronal Networks, Department of Biology, University of Kaiserslautern, Kaiserslautern, Germany

³Electrical & Computer Engineering, University of Delaware, Newark, Delaware, USA

Edited by: Ian Forsythe & Samuel Young

The peer review history is available in the supporting information section of this article (<https://doi.org/10.1113/JP280403#support-information-section>).



Nicolas Müller received his PhD in 2019. He investigated developmental circuit refinement and synaptic performance of the MNTB–LSO projection upon peripheral and central manipulations of the auditory system. By doing so, he gained mechanistic insight into the maturation of inhibitory synapses. He recently headed to industry and now works as a data scientist focusing on non-invasive detection of brain disorders.



Abstract Sound localization involves information analysis in the lateral superior olive (LSO), a conspicuous nucleus in the mammalian auditory brainstem. LSO neurons weigh interaural level differences (ILDs) through precise integration of glutamatergic excitation from the cochlear nucleus (CN) and glycinergic inhibition from the medial nucleus of the trapezoid body (MNTB). Sound sources can be localized even during sustained perception, an accomplishment that requires robust neurotransmission. Virtually nothing is known about the sustained performance and the temporal precision of MNTB–LSO inputs after postnatal day (P)12 (time of hearing onset) and whether acoustic experience guides development. Here we performed whole-cell patch-clamp recordings to investigate neurotransmission of single MNTB–LSO fibres upon sustained electrical stimulation (1–200 Hz/60 s) at P11 and P38 in wild-type (WT) and deaf otoferlin (*Otof*) knock-out (KO) mice. At P11, WT and KO inputs performed remarkably similarly. In WTs, the performance increased drastically between P11 and P38, e.g. manifested by an 8 to 11-fold higher replenishment rate (RR) of synaptic vesicles and action potential robustness. Together, these changes resulted in reliable and highly precise neurotransmission at frequencies ≤ 100 Hz. In contrast, KO inputs performed similarly at both ages, implying impaired synaptic maturation. Computational modelling confirmed the empirical observations and established a reduced RR per release site for P38 KOs. In conclusion, acoustic experience appears to contribute massively to the development of reliable neurotransmission, thereby forming the basis for effective ILD detection. Collectively, our results provide novel insights into experience-dependent maturation of inhibitory neurotransmission and auditory circuits at the synaptic level.

(Received 5 July 2020; accepted after revision 30 March 2022; first published online 19 April 2022)

Corresponding author Eckhard Friauf, Animal Physiology Group, Department of Biology, University of Kaiserslautern, Kaiserslautern, Germany. Email: eckhard.friauf@bio.uni-kl.de

Abstract figure legend MNTB–LSO inputs are a major component of the mammalian auditory brainstem. Reliable neurotransmission at these inputs requires both failure-free conduction of action potentials and robust synaptic transmission. The development of reliable neurotransmission depends crucially on functional hearing, as demonstrated in a time series and by the fact that deafness – upon loss of the protein otoferlin – results in severely impaired synaptic release and replenishment machineries. These findings from animal research may have some implications towards optimizing cochlear implant strategies in newborn humans.

Key points

- Inhibitory glycinergic inputs from the medial nucleus of the trapezoid body (MNTB) to the lateral superior olive (LSO) are involved in sound localization. This brainstem circuit performs reliably throughout life. How such reliability develops is unknown.
- Here we investigated the role of acoustic experience on the functional maturation of MNTB–LSO inputs at juvenile (postnatal day P11) and young adult ages (P38) employing deaf mice lacking otoferlin (KO).
- We analysed neurotransmission at single MNTB–LSO fibres in acute brainstem slices employing prolonged high-frequency stimulation (1–200 Hz/60 s).
- At P11, KO inputs still performed normally, as manifested by normal synaptic attenuation, fidelity, replenishment rate, temporal precision and action potential robustness. Between P11 and P38, several synaptic parameters increased substantially in wild-type mice, collectively resulting in high-fidelity and temporally precise neurotransmission. In contrast, maturation of synaptic fidelity was largely absent in KOs after P11.
- Collectively, reliable neurotransmission at inhibitory MNTB–LSO inputs develops under the guidance of acoustic experience.

Introduction

Sensory circuits allow animals to perceive their environment throughout life. This is a challenging task for the auditory system because (1) acoustic stimulation is virtually continuous in nature (Lalor et al., 2009), (2) synapses must cope with extraordinarily high activation rates (Taschenberger & von Gersdorff, 2000), and (3) neurotransmission must occur with high fidelity and precision for faithfully encoding sound (Oertel, 1999; Trussell, 1999). The challenges are especially evident in the sound localization nuclei of the superior olivary complex (SOC), such as the lateral superior olive (LSO). LSO principal neurons compute interaural level differences (ILDs) via integrating excitatory (glutamatergic) input from the cochlear nucleus (CN) and inhibitory (glycinergic) input from the medial nucleus of the trapezoid body (MNTB) (Ashida et al., 2017; Beiderbeck et al., 2018; Boudreau & Tsuchitani, 1968; Caird & Klinke, 1983; Fischer et al., 2019; Franken et al., 2018; Glendenning et al., 1985; Joris & van der Heijden, 2019; recent reviews: Friauf et al., 2019; Owruksy et al., 2021).

MNTB–LSO synapses are formed by axonal boutons that are larger than classical bouton terminals (Gjoni, Aguet et al., 2018; Helfert & Schwartz, 1986) yet still much smaller than endbulb or calyx of Held synapses. They are also inconspicuous compared with the highly specialized morphology of ribbon synapses at inner hair cells (Yu & Goodrich, 2014). The facts that MNTB-mediated inhibition is crucial for proper ILD analysis (Beiderbeck et al., 2018; Grothe & Pecka, 2014; Masterton et al., 1967) and that sound sources are reliably localized even against noisy backgrounds (Kerber & Seeber, 2012) argue for extraordinarily robust neurotransmission, despite the bouton-type terminals. Indeed, MNTB–LSO synapses of P11 mice perform more reliably upon sustained high-frequency stimulation *in vitro* than other auditory and non-auditory bouton-type synapses (Brill et al., 2019; Krächan et al., 2017). Virtually nothing is known about the *sustained* neurotransmission behaviour after P11, including the question of whether this parameter matures further and, if so, which mechanisms determine maturation.

Mice are physiologically deaf until ~P12 (the age of hearing onset; Ehret, 1976, 1983). Thereafter, acoustic experience further shapes auditory brainstem circuits (Cao et al., 2008; Kandler et al., 2009; Magnusson et al., 2005; Pilati et al., 2016; Sanes & Takacs, 1993; Wright et al., 2014), but the impact of acoustic experience on the development of sustained synaptic performance has not been investigated so far. To address this issue, we employ a deafness mouse model lacking functional otoferlin (*Otof* KOs; Longo-Guess et al., 2007). *Otof* is a Ca^{2+} -sensing protein that mediates synaptic vesicle (SV) exocytosis

from inner hair cells (Beurg et al., 2009; Heidrych et al., 2009; Michalski et al., 2017). Consequently, mutations of *OTOF* in humans (Mahdiah et al., 2012; Pangrsic et al., 2012; Petersen & Willems, 2006) and mutations of *Otof* in mice (Longo-Guess et al., 2007; Roux et al., 2006) typically cause deafness due to auditory synaptopathy (Moser & Starr, 2016; Starr & Rance, 2015). *Otof* expression is high in the inner ear (Roux et al., 2006), but absent in the MNTB and LSO (Müller et al., 2019), therewith highlighting the impact of synaptic transmission from inner hair cells. Disturbed synaptic transmission in *Otof* KOs disrupts spontaneous prehearing activity and affects MNTB–LSO circuitry; more, yet functionally weaker MNTB fibres converge on a single LSO neuron (Müller et al., 2019). In line with this, *Otof* KOs also show impaired ultrastructural morphology at endbulb of Held synapses (Hintze et al., 2021). Furthermore, developing auditory cortex circuits are altered in *Otof* KOs (Mukherjee et al., 2021).

Here we analysed the robustness and temporal precision of MNTB–LSO inputs in developing WT and *Otof* KOs. Using *Otof* KOs, we evaluated the impact of disrupted spontaneous activity and acoustic experience on the maturation of neurotransmission. To do so, we electrically stimulated single MNTB fibres in minimal stimulation experiments (1–200 Hz/60 s) and recorded evoked inhibitory postsynaptic currents (eIPSCs) from LSO principal neurons in acute slices from P11 and P38 WT and age-matched *Otof* KOs.

Sustained MNTB fibre stimulation at P11 resulted in similar synaptic attenuation, fidelity, replenishment rate (RR) and temporal precision in WT and *Otof* KOs. Moreover, action potential (AP) failures occurred at a rate of >66% in each genotype during sustained high-frequency stimulation. In P38 WT, single MNTB fibres performed virtually failure-free, and neurotransmission was highly precise during 60 s challenge periods at ≤ 100 Hz. Furthermore, high fidelity and precision were achieved by a drastic increase of the RR between P11 and P38 (8 to 11-fold). In contrast, single fibre fidelity in P38 *Otof* KOs remained as low as at P11. Both genotypes displayed similar maturation of AP fidelity between P11 and P38. The reduced neurotransmission fidelity of P38 *Otof* KOs was not due to a smaller readily releasable pool (RRP), reduced MNTB fibre excitability, altered eIPSC-to-noise ratio in failure detection, or insufficient recovery between high-frequency trains. Instead, the reduced fidelity can be explained by a virtual lack of an age-dependent RR increase. We further validated our empirical results by computational modelling, which established a reduced RR per release site in P38 *Otof* KOs.

Taken together, we demonstrate an age-dependent increase of neurotransmission performance in WT that is due to a drastic increase in SV replenishment. Such an increase is largely absent in deaf *Otof* KOs. In

contrast, AP fidelity appears to develop normally in *Otof* KOs. Collectively, our findings demonstrate that the maturation of reliable neurotransmission in the central auditory system (MNTB–LSO inputs) during ongoing high-frequency stimulation requires acoustically driven synaptic transmission in the cochlea which may thus ensure proper ILD coding.

Methods

Animals and ethical approval

Animal breeding and experiments were approved by the regional councils of the Land Rhineland-Palatinate according to the German Animal Protection Law (TSchG §4/3) and followed the guidelines for the welfare of laboratory animals. The authors understand and conform to the principles and regulations described in *The Journal of Physiology* (Grundy, 2015). Experiments were performed on *Otof*^{deaf5/deaf5} mice (Longo-Guess et al., 2007) and age-matched control (*Otof*^{f+/+}) mice of both sexes, which were bred in the animal facility of the University of Kaiserslautern. The mice had a mixed C57BL/6J, CH3 background and were genotyped as described previously (Longo-Guess et al., 2007). *Otof*^{f+/+} and *Otof*^{deaf5/deaf5} mice were typically littermates. Throughout the paper, *Otof*^{deaf5/deaf5} mice are designated ‘*Otof* KOs’ or ‘KOs’. *Otof*^{f+/+} mice are designated ‘WTs’. *n* corresponds to the number of recorded cells.

Electrophysiology

Coronal brainstem slices of P10–12 (designated P11) mice were prepared as described (Krächan et al., 2017). We adopted a protocol from Ting and colleagues (2014) to prepare viable brainstem slices from young adult animals (P31–49, labelled P38). The procedure has been described previously (Müller et al., 2019). Mice were injected with a lethal dose of ketamine hydrochloride (10 mg per animal intraperitoneally), decapitated and their brains were rapidly removed. Slices were stored for 0.5–5 h at room temperature in artificial cerebrospinal fluid containing (in mM): 125 NaCl, 2.5 KCl, 1 MgCl₂, 1.25 NaH₂PO₄, 2 Na-pyruvate, 3 myo-inositol, 0.44 L-ascorbic acid, 25 NaHCO₃, 10 D-glucose, 2 CaCl₂ (pH 7.4 when bubbled with carbogen; 295 ± 5 mosmol/L). Thereafter, slices were transferred to the recording chamber mounted on an upright microscope (Eclipse E600N, Nikon, Tokyo, Japan) equipped with infrared-differential interference contrast (DIC) optics (Nikon 4× CFI Achromat, 0.1 ∞; 60× CFI Fluor W, 1.00 W ∞) and a VX 44 CCD camera (PCO computer optics, Kehlheim, Germany). Patch pipettes were pulled from glass capillaries (GB150(F)–8P, Science Products, Hofheim am Taunus, Germany) with a P-87 horizontal puller (Sutter Instruments, Novato, CA,

USA). Tip resistances ranged from 2 to 5 MΩ when filled with internal solution containing (in mM): 140 K-gluconate, 10 Hepes, 5 EGTA, 1 MgCl₂, 2 Na₂ATP, 0.3 Na₂GTP (280 ± 10 mosmol/L). The chloride reversal potential at 37°C was -112 mV. The liquid junction potential (15.4 mV) was corrected online. Whole-cell patch-clamp recordings ($V_{\text{hold}} = -70$ mV, resulting in an inward-directed driving force for Cl⁻ of 42 mV and thus in outward currents) were performed using an EPC9 amplifier and Patchmaster software (HEKA, Lambrecht/Pfalz, Germany). LSO neurons with fusiform somata were chosen and confirmed as principal neurons by their electrophysiological properties (Sternborg et al., 2010). Recordings were sampled at 20 kHz and low-pass filtered at 2.9 kHz. Series resistances ranged from 6 to 20 MΩ and were compensated between 20 and 60% (higher series resistances were compensated with a higher percentage). If the input resistance changed >30%, recordings were discarded. All experiments were performed at 36.5 ± 1°C (Slice Mini Chamber I equipped with a temperature controller TC05, Luigs & Neumann, Ratingen, Germany).

Electrical stimulation of MNTB fibres: orthodromic activation

A stimulation electrode (glass capillary, ~10 μm tip diameter) was connected to a stimulus isolator (STG 4002, Multi-Channel Systems, Reutlingen, Germany) and placed at the lateral edge of the MNTB. To stimulate MNTB fibres in a stepwise manner, the stimulus amplitude was increased in small increments of 5 μA, repeated 10 times. Monopolar stimulus pulses of 100 μs were applied. Synaptic depression was avoided by stimulating at 0.5 Hz. Single MNTB fibre recruitment (minimal stimulation) was achieved when stimulation resulted in eIPSCs at the LSO principal neuron (see Fig. 1*Ca* and *b*). Subsequent stimulus amplitudes were also tested to determine a range of suitable stimulus amplitudes for minimal stimulation (see Fig. 1*D*). If 5 μA steps were too big to resolve a suitable stimulus amplitude for consistent single fibre stimulation (e.g. by recruitment of an additional fibre), manual adjustments of the stimulus amplitude were made within the 5 μA increment until a reliable single fibre stimulation was achieved (tested with ~10 sweeps). Inconsistent stimulation of MNTB fibres was obvious in ‘jumps’ of eIPSC amplitude and was typically noticed online. In such cases, the attempt to find a suitable stimulus amplitude for single fibre stimulation was repeated. If an inconsistent fibre recruitment was unnoticed online, jumps of eIPSC peak amplitudes were assessed offline. Recordings with an inconsistent fibre number were excluded from the analysis. The minimal stimulation paradigm at P38 was largely performed on the same cells as in the previous study (Müller et al., 2019).

The minimal stimulation paradigm at P11, however, was performed independently from this previous study.

Stimulation of all converging MNTB fibres (maximal stimulation) was achieved using stimulus amplitudes which yielded maximal eIPSC amplitudes, i.e. amplitudes saturated upon further increase of the stimulus amplitude. Stimulus amplitudes for maximal stimulation were consistent with previous studies (Clause et al., 2014; Hirtz et al., 2012; Kim & Kandler, 2003, 2010; Lee et al., 2016; Müller et al., 2019; Noh et al., 2010).

Sustained stimulation of MNTB fibres started with a 60 s baseline normalization period and stimulation at 0.2 Hz. Subsequently, a 60 s challenge was followed by 60 s recovery. The stimulus frequency during challenge was increased (1, 2, 5, 10, 20, 50, 100, 200 Hz), whereas it was constantly 1 Hz during recovery. A total of 23,760 stimuli were given throughout such a protocol. A 10 s pause was introduced between the last stimulus of a recovery period and the first stimulus of a subsequent challenge period in order to store data. The sustained stimulation protocol was used for minimal stimulation at P11 and P38 (Figs 2, 3, 5, 6, 8 to 15) and for maximal stimulation at P38 (Fig. 7). Maximal stimulation at 100 Hz for 1 s (20 repeats, 20 s pause in between) was performed in WTs and *Otof* KOs at P11 and P38 (Fig. 8, traces are averages of 20 repeats).

Assessment of AP fidelity of MNTB fibres: antidromic stimulation experiments

We assessed the capability of MNTB neurons to reliably generate and conduct APs along their axons during sustained high-frequency challenge. For that purpose, we obtained somatic current-clamp recordings from MNTB neurons and electrically stimulated their axons at the medial edge of the LSO to elicit antidromic APs. Experimental conditions (electrophysiology set-up, stimulus isolator, stimulation pipettes) were the same as for orthodromic stimulation, except for the sample frequency (50 kHz). The stimulus amplitude was set to a twofold threshold. Each 60 s challenge period (1, 10, 50, 100, 200 Hz) was followed by a 1 Hz 60 s recovery period.

Data analysis

Peak amplitudes of eIPSCs were analysed with custom-written routines (Dr Alexander Fischer, University of Kaiserslautern) for IGOR Pro (Wavemetrics, Lake Oswego, OR, USA) running Patcher's Power Tools (Max Planck-Institute for Membrane Biophysics). The mean eIPSC peak amplitude during the 0.2 Hz for 60 s normalization period was set to 100% and used for normalization. eIPSC peak amplitudes ≤ 1.5 times the quantal size (q) were considered as synaptic failures. Such failures corresponded to a fidelity of 0, and eIPSC

amplitudes ≥ 1.5 times q to a fidelity of 1. For the fidelity analysis, we globally set q to 22 pA as determined previously (Krächan et al., 2017; Müller et al., 2019). Notice that our ' $1.5 \times q$ ' criterion is conservative and results in an underestimated number of released SVs.

To quantify the frequency dependence of eIPSC amplitudes (Figs 2Cc and 3Cc), we fitted the data by Hill functions. Hill functions were also used for the fidelity rate (Figs 2Dc and 3DC) and the AP failure rate (Fig. 4C).

Voltage traces from antidromic stimulation experiments were analysed for AP fidelity. MNTB neurons displaying $V_{\text{rest}} < -60$ mV were included in the analysis. APs were detected by a threshold-based search (peak amplitude ≥ -50 mV).

The RRP-related current (I_{RRP}) was determined using the method of Elmqvist & Quastel (1965). The number of SVs in the RRP (N_{RRP}) was determined by dividing the I_{RRP} by the respective q of each cell. We derived q from distributions of spontaneous IPSC amplitudes (Brill et al., 2019; Krächan et al., 2017; Müller et al., 2019) and Gaussian fitting incorporated into Excel spreadsheets (Kemmer & Keller, 2010). The initial release probability (P_v) was determined by dividing the number of released SVs at the first eIPSC by the N_{RRP} . The replenishment was determined by cumulative summation of all eIPSC amplitudes during a 100 Hz for 60 s train. The slope of a linear fit during seconds 50 to 60 (s_{50-60}) was used to calculate RR in absolute current (Körber et al., 2015; Mendoza Schulz et al., 2014; Parthier et al., 2018; Wen et al., 2016). Division by q yielded the RR in SVs/stimulus (interstimulus interval at 100 Hz = 0.01 s), which was converted to SVs/s (*cf.* Fig. 9B).

Latencies were determined as the time from the peak of the stimulation artefact to the peak of the eIPSC using custom-written IGOR routines. Synaptic failures were excluded from the latency analysis. The standard deviation of the latency (latency SD) served as a measure of synaptic precision (Brill et al., 2019; Krächan et al., 2017). In the sustained stimulation protocol, the latency SD was determined during s_{50-60} for individual recordings. Latency and precision analyses were omitted at P11 for frequencies > 50 Hz due to the high number of failures during s_{50-60} (*cf.* Fig. 2D). All experiments and analyses were performed blind to the genotype.

Computational modelling

We applied a deterministic model that considers M release sites (subsequently named 'sites'), where each site is either occupied by an SV or empty. An empty site is reoccupied at a replenishment rate RR_i between the i^{th} and $(i+1)^{\text{th}}$ stimulus. $N_{\text{RRP}i}$ denotes the number of occupied sites just before the arrival of the i^{th} AP, and P_v is the probability of SV fusion upon an AP. We assume that all sites are

occupied at rest (Neher, 2017), i.e. there is no empty site at the start of the challenge ($M = N_{RRP1}$). Further,

$$N_{RRPi} \times P_v = m_i \quad (1)$$

$$N_{RRPi+1} = N_{RRPi} \times (1 - P_v) + (M - N_{RRPi} \times (1 - P_v)) \times \left(1 - e^{-\frac{RR_i}{f}}\right) \quad (2)$$

where m_i is the number of SVs released in response to the i^{th} stimulus (= quantal content) and f is the stimulus frequency (100 Hz).

The term $N_{RRPi+1} = N_{RRPi} \times (1 - P_v)$ represents N_{RRP} depletion in response to the i^{th} stimulus, and the term $(M - N_{RRPi} \times (1 - P_v)) \times (1 - e^{-\frac{RR_i}{f}})$ represents the RR between the i^{th} and the $i+1^{\text{th}}$ stimulus, with $M - N_{RRPi} \times (1 - P_v) = M - N_{RRPi} + N_{RRPi} \times P_v$ depicting the number of empty sites directly after SV release to the i^{th} stimulus and $(M - N_{RRPi} + N_{RRPi} \times P_v) \times (1 - e^{-\frac{RR_i}{f}})$ depicting the decrease of empty sites through replenishment.

We assume that RR builds up initially (Weingarten, 2018) such that RR_1 , RR_2 and RR_3 differ. To obtain basic parameters and starting with the fourth stimulus, we assume that RR remains constant during the first second, namely $RR_i = RR_4$. The model parameters M , P_v , RR_1 , RR_2 , RR_3 and RR_4 are estimated by performing least-square fitting with the averaged empirical data for the first second. To predict long-term SV release, we assume that RR decreases monotonically as per a double exponential decay via

$$RR_i = RR_{\min} + (RR_4 - RR_{\min}) \times \left(g \times e^{-\frac{i-Delay}{\tau_1}} + (1-g) \times e^{-\frac{i-Delay}{\tau_2}}\right) \quad (3)$$

if stimulus $i > Delay$. τ_1 and τ_2 are decay time constants for RR, g is a constant, and RR_{\min} is the minimum replenishment rate after a very large number of stimuli (going to infinity). If $i < Delay$, RR is assumed to be constant and equal to RR_4 . τ_1 , τ_2 , g , $Delay$ and RR_{\min} are determined by fitting the model to the number of SVs released for the entire challenge period (all 6000 stimuli).

To model replenishment during recovery periods, we again use equations (1) and (2), but with $f = 1$ Hz. RR is assumed to increase monotonically during each recovery period as per the following equation:

$$RR_i = RR_{recmax} + (RR_{recmin} - RR_{recmax}) \times e^{-\frac{i-6000}{\tau_{rec}}}; 6001 \leq i \leq 6060 \quad (4)$$

RR_{recmax} , RR_{recmin} and τ_{rec} are estimated by fitting the model to the empirically obtained recovery data.

To consider AP failures in MNTB neurons and their stochastic nature, we slightly modified equation (2) by

changing the stimulus frequency f to f_i , i.e. to an instantaneous frequency. In the presence of one failure between two successful events and with $f = 100$ Hz, $f_i = 50$ Hz and in the presence of two failures, $f_i = 33$ Hz, etc. We applied the modified model to generate Fig. 11. Note that several processes addressed in our models, such as quantal content, SV release, or the RR, are discrete processes in reality. Therefore, our discontinuous model variables ought to be discrete integer values in *sensu stricto*. However, for simplicity, we replaced them with continuous parameters (see also Neher, 2017).

Statistics

Sample data are presented as means \pm SD. Statistical analysis was performed with Origin Pro 8.6 (OriginLab, Northampton, MA, USA). Normally distributed samples (Kolmogorov–Smirnov) were compared in paired or unpaired two-tailed t tests. A homo- or heteroskedastic t test was performed based on the equality of variances determined by an F test. If data were not normally distributed, a Mann–Whitney U test was applied. In case of multiple comparison, critical α values were *post hoc* Šidák corrected (Abdi, 2007).

Significance levels were then:

Significance level	Number of comparisons (k)		
	1	2	3
*	0.05	0.025	0.017
**	0.01	0.005	0.0033
***	0.001	0.0005	0.00033

Results

Neurotransmission between auditory brainstem neurons is highly resistant to fatigue. Synaptic inputs show remarkable fidelity and high temporal precision, even when activated hundreds of times per second (Brill et al., 2019; Friauf et al., 2015; Krächan et al., 2017; Sonntag et al., 2011; Taschenberger & von Gersdorff, 2000). In the present study, we investigated whether the neurotransmission fidelity of MNTB–LSO inputs matures after hearing onset and if so, whether the maturation requires acoustic experience.

No developmental fidelity increases for sustained neurotransmission in *Otof* KOs

In a previous paper (Müller et al., 2019), we described impaired circuit refinement in *Otof* KOs, evidenced by

more – yet weaker – MNTB fibres converging on a single LSO principal neuron (*cf.* Fig. 1Aa in the present study). To ensure comparability between WT and *Otof* KOs, we here conducted single MNTB fibre stimulation (= minimal stimulation; Fig. 1Ab). Very low stimulus amplitudes failed to elicit an eIPSC, yet amplitude increases in small increments ultimately resulted in activation of a single MNTB fibre and reliable eIPSCs (Fig. 1B–D). For further neurotransmission analysis, we chose a suitable stimulus amplitude from the range of stimulus amplitudes at which stable single fibre activation was achieved (Fig. 1D). Under these conditions, mean eIPSC peak amplitudes were: P11 WT: 253 ± 32 pA; P11

Otof KOs: 156 ± 26 pA; P38 WT: 470 ± 56 pA; P38 *Otof* KOs: 160 ± 36 pA (Fig. 1E and F; $n = 11, 12, 13, 11$). The results are consistent with those presented earlier (Müller et al., 2019).

Having determined the suitable stimulus amplitude, we assessed the neurotransmission behaviour of single MNTB fibres during sustained minimal stimulation (1–200 Hz/60 s). For the two genotypes, current traces from a P11 MNTB–LSO input at 1, 10 and 100 Hz are shown in Fig. 2A and B. With increasing frequency, synaptic attenuation (for definition, see Friauf et al., 2015) increased similarly in WT and *Otof* KOs (s_{50-60} ; Table 1). Steady-state attenuation for WT and *Otof* KOs reached

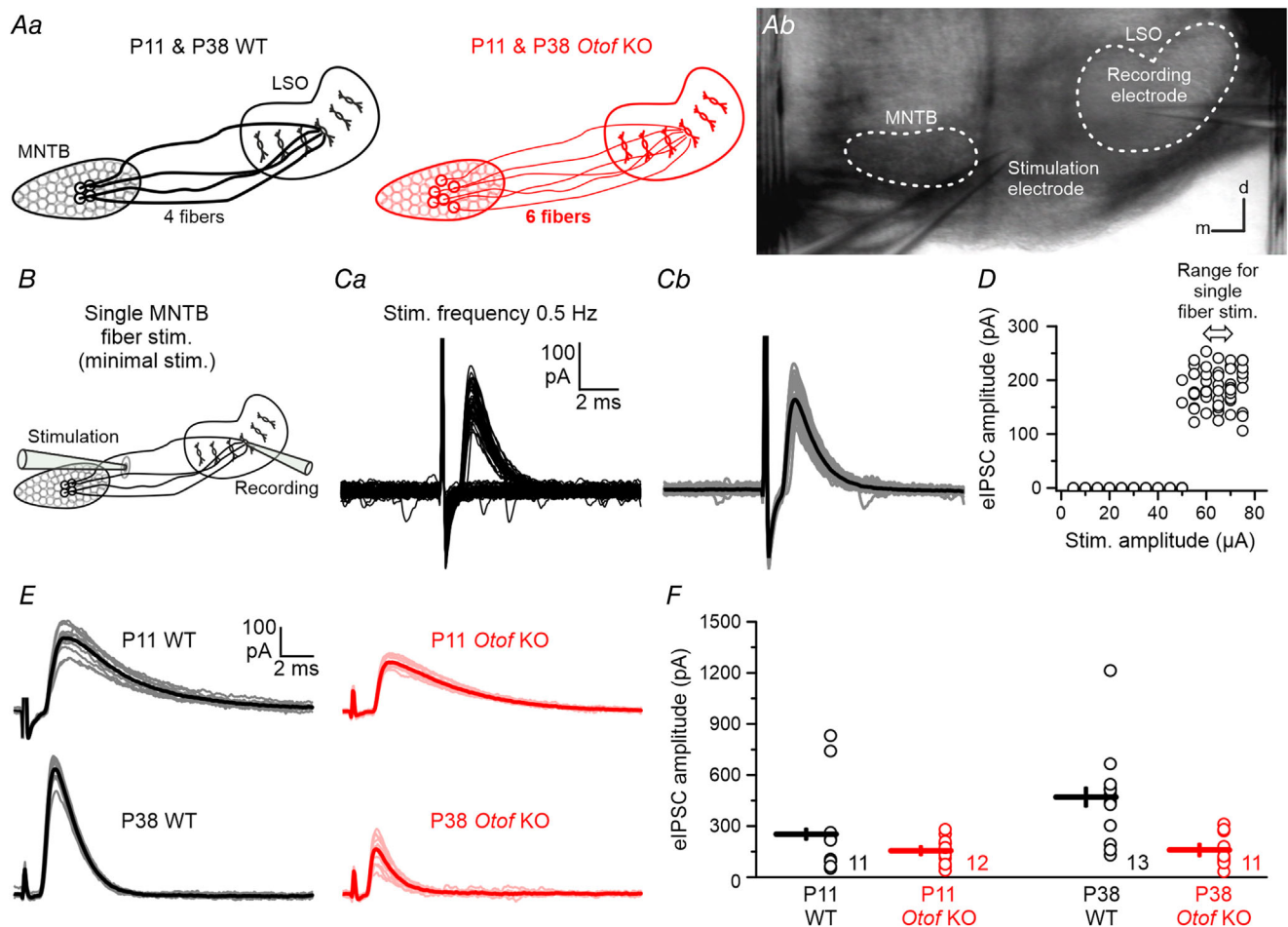


Figure 1. MNTB–LSO circuit and single fibre stimulation

Aa, schemes of the MNTB–LSO circuitry in WT and *Otof* KOs. Notice unrefined connectivity in *Otof* KOs. Ab, differential interference contrast image of a coronal slice containing the MNTB and the LSO, with stimulation electrode and recording electrode in place. Medial (m) and dorsal (d) calibration bar: $100 \mu\text{m}$. B, scheme of single MNTB fibre stimulation. Circles around stimulation electrode indicate various stimulus amplitudes. C, the stimulus amplitude was increased in small increments (Ca) until IPSCs were consistently evoked (Cb, same as in Ca but with failures excluded; grey traces: individual eIPSCs; black trace: graphical mean). D, eIPSC peak amplitudes as a function of stimulus amplitude. Double arrow marks range of stimulus amplitudes suitable for stable single fibre stimulation. E, eIPSCs from WT and *Otof* KO LSO neurons at P11 and P38, each evoked by a single MNTB fibre. Thin traces: 12 individual eIPSCs; thick trace: graphical mean. F, sample data for eIPSC amplitudes. Numbers in plot are cell numbers. eIPSC: evoked inhibitory post-synaptic currents; IPSC: inhibitory post-synaptic current; KO: knock-out; LSO: lateral superior olive; MNTB: medial nucleus of the trapezoid body; WT: wild type.

~80% of the normalized eIPSC amplitude at 1 Hz, ~50% at 10 Hz, and ~10% at 100 Hz, resulting in 50% depression frequencies ($f_{50\text{Amp}}$) of 8 and 10 Hz, respectively (Fig. 2C; Table 1). At each frequency, steady-state attenuation did not differ between WTs and *Otof* KOs (Fig. 2C; Table 1). Neurotransmission failures occurred similarly often in WTs and *Otof* KOs at the end of 60 s challenge periods (Fig. 2Ac and Bc), revealing similar fidelity rates for a given frequency (Fig. 2D; Table 2).

To assess developmental changes in the fidelity of sustained neurotransmission, we next performed minimal stimulation experiments at P38, an adult-like age so far unexplored in either genotype. Example current traces at 1, 10 and 100 Hz are shown in Fig. 3A and B. As at P11, synaptic attenuation increased in a frequency-dependent

manner (Fig. 3Ca and b; Table 1). Steady-state amplitudes for WTs and *Otof* KOs at s₅₀₋₆₀ were ~80% at 1 Hz, ~50% at 10 Hz and ~20% at 100 Hz, resulting in similar $f_{50\text{Amp}}$ values of 9 and 10 Hz, respectively (Fig. 3Cc). In each genotype, the majority of steady-state amplitudes was statistically indistinguishable at both P11 and P38 (12/16 frequencies, Table 1). At P38, neurotransmission in WTs was virtually failure-free up to 50 Hz (Fig. 3Ac, Da and c; Tables 1 and 2). In contrast, neurotransmission failures already occurred at 5 Hz in *Otof* KOs (Fig. 3Db and c; Table 2). Accordingly, significantly more failures took place in P38 *Otof* KOs at ≥ 10 Hz, resulting in a 50% fidelity frequency ($f_{50\text{TotFid}}$) of 150 Hz for WTs and 41 Hz for *Otof* KOs (Fig. 3Dc; Table 2). Between P11 and P38, neurotransmission fidelity ≥ 20 Hz increased considerably in

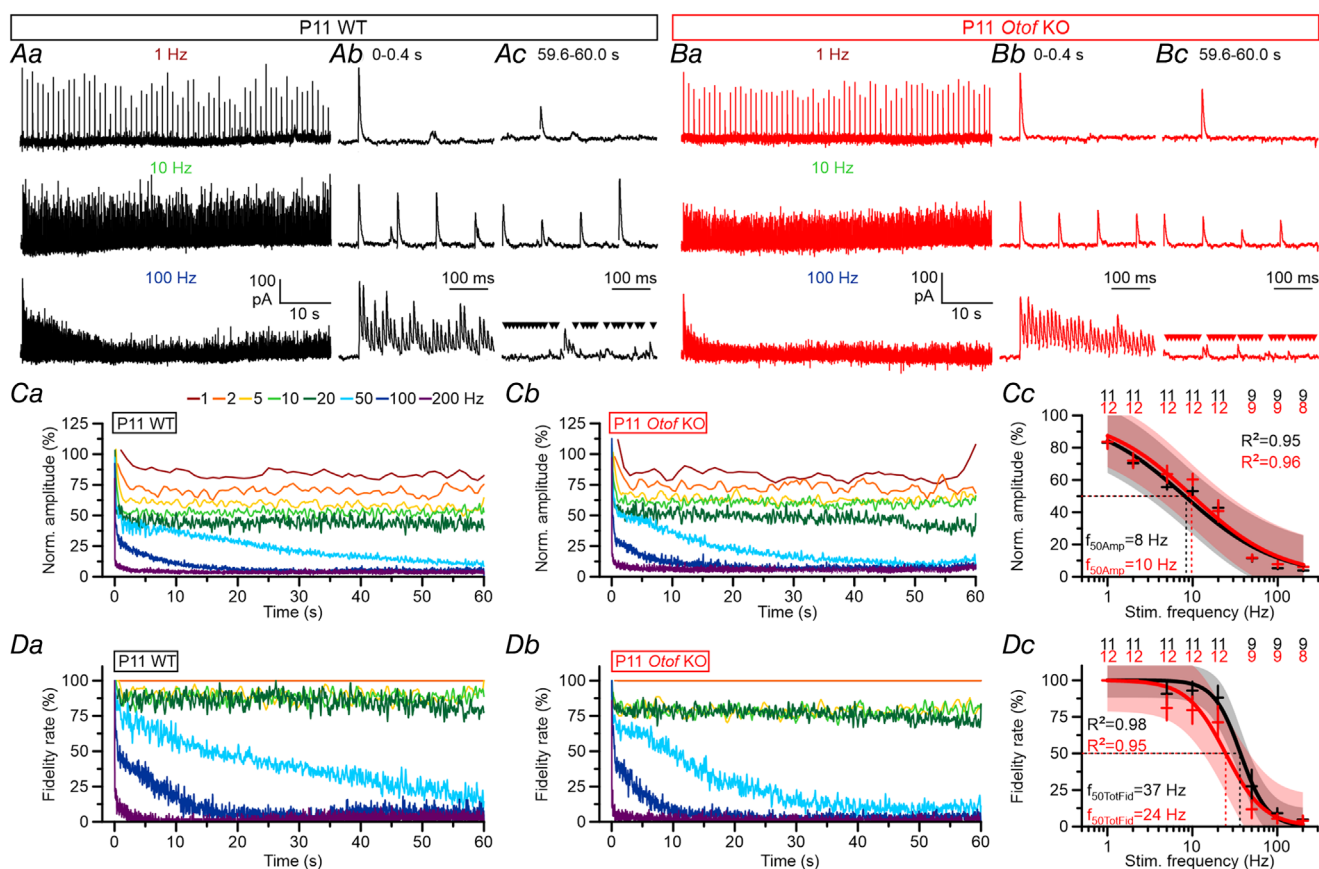


Figure 2. Normal transmission fidelity in P11 *Otof* KO neurons

A, B, eIPSCs of a P11 WT (A) and an *Otof* KO neuron (B) during 60 s challenge of single MNTB fibres at 1, 10 and 100 Hz (Aa, Ba) and respective close-ups at the trains' start (s_{0-0.4}; Ab, Bb) or end (s_{59.6-60.0}; Ac, Bc). Triangles above traces mark synaptic failures. Ca, Cb, time course of mean normalized eIPSC amplitudes in P11 WTs (Ca) and *Otof* KOs (Cb). Cc, frequency dependence of mean normalized amplitude during s₅₀₋₆₀. Da–c, as C, but for fidelity. Time courses in Ca–Cb and Da–Db are parabolic weighted moving averages of three (1–2 Hz), five (5–20 Hz), or nine data points (50–200 Hz). Fits in Cc and Dc are sigmoidal regressions. Minimum and maximum values were set to 0 and 1, respectively. Shaded areas depict 95% confidence intervals. $f_{50\text{Amp}}$ and $f_{50\text{TotFid}}$ values (stippled lines) were determined from sigmoidal regressions. Notice that $f_{50\text{TotFid}}$ reflects the fidelity of both action potential conduction and synaptic transmission. Numbers above plots are number of cells. Statistical comparison of normalized amplitude and fidelity between WTs and *Otof* KOs was done via an unpaired two-tailed *t* test, except for fidelity at 1–5 Hz (*U* test). Details in Tables 1 and 2. eIPSC: evoked inhibitory post-synaptic currents; KO: knock-out; MNTB: medial nucleus of the trapezoid body; WT: wild type.

Table 1. Steady-state eIPSC amplitudes in WT and *Otof* KOs at P11 and P38

		Stimulation frequency (Hz)							
		1	2	5	10	20	50	100	200
eIPSC amplitude s_{50-60} (%)	P11	79 ± 14	71 ± 7	57 ± 5	54 ± 6	41 ± 9	12 ± 6	6 ± 2	4 ± 1
	WT	(11)	(11)	(11)	(11)	(11)	(9)	(9)	(9)
	P11	83 ± 16	72 ± 16	62 ± 18	60 ± 12	40 ± 23	11 ± 5	7 ± 6	5 ± 3
	<i>Otof</i> KO	(12)	(12)	(12)	(12)	(12)	(9)	(9)	(9)
P value WT vs. KO		0.52	0.95	0.38	0.21	0.99	0.81	0.60	0.62
eIPSC amplitude s_{50-60} (%)	P38	78 ± 8	66 ± 10	54 ± 9	48 ± 5	46 ± 14	33 ± 11	19 ± 7	8 ± 4
	WT	(13)	(13)	(13)	(13)	(12)	(12)	(12)	(12)
	P38	80 ± 12	70 ± 13	57 ± 10	57 ± 17	43 ± 14	32 ± 14	12 ± 8	7 ± 4
	<i>Otof</i> KO	(11)	(11)	(11)	(11)	(10)	(10)	(10)	(9)
P value WT vs. KO		0.61	0.47	0.43	0.12	0.76	0.73	0.07	0.58
P value P11 vs. P38 WT		0.89	0.23	0.36	0.41	0.31	5.5E-5	7.6E-05	0.02
P value P11 vs. P38 KO		0.74	0.89	0.51	0.65	0.80	0.002	0.20	0.48

Normalized amplitude values (means ± SD) were determined during s_{50-60} of each challenge period (cf. Figs 2 and 3). 100% represents the baseline value. Values in brackets depict number of cells. *P* values were determined by an unpaired two-tailed *t* test. eIPSC: evoked inhibitory post-synaptic current; KO: knock-out; WT: wild type.

WTs (Table 2). By contrast, such a developmental increase was largely absent from *Otof* KOs, resulting in similar fidelity values for both ages (6/8 frequencies, Table 2). Likewise, $f_{50\text{TotFid}}$ increased less than 1.7-fold with age in *Otof* KOs, compared with >4-fold in WT (Figs 2Dc and 3Dc; Table 2).

Taken together, neurotransmission fidelity does not differ between WT and *Otof* KOs at hearing onset. Fidelity increases strongly in WT with acoustic experience as evidenced by highly reliable neurotransmission at P38, even during sustained high-frequency challenge. In contrast, the fidelity remains immature in *Otof* KOs, implying that acoustic experience is essential for developing robust and failure-free neurotransmission.

AP fidelity of MNTB neurons

Neurotransmission failures may have two reasons. First, axon terminals may be unable to release transmitter-filled SVs, which results in synaptic failures. Second, pre-synaptic neurons may be unable to elicit APs and/or to reliably conduct them into the axon terminals; for example, because of reduced excitability caused by Na_v channel inactivation (Ulbricht, 2005). To address the second reason, namely, reduced AP fidelity, we performed antidromic stimulation experiments in which we recorded from individual MNTB somata while electrically stimulating their axon at the medial border of the LSO, akin to a previous study (Kramer et al., 2014). Challenge periods lasted 60 s and comprised several frequencies (1–200 Hz). Figure 4Aa–Ad shows original voltage recordings with successful APs and

failures obtained from four representative neurons, panels *Ba–Bd* show dot plots, and panels *Ca–Cd* show the failure rate as a function of the stimulation frequency. Upon 100 Hz challenge, P11 WT MNTB neurons displayed a mean AP failure rate of $66 \pm 32\%$ during s_{50-60} (range: 0–100%; $n = 14$, one of them failure-free; Fig. 4Aa–Ca and D). Although this implies considerable limitations of AP generation and/or propagation at the end of 100 Hz challenge, the value is significantly lower than the total failure rate of $93 \pm 7\%$ (Table 2 and Fig. 4D; see also Fig. 2Da and Dc). Neurotransmission comprises AP propagation and SV release (total failures = AP failures + synaptic failures). Consequently, the difference 93% – 66% suggests that limitations in the terminal axon boutons contribute by 27% to the high total failure rate of 93%, i.e. by more than a quarter (Fig. 4E). We reason that such limitations comprise insufficient SV replenishment and/or SV exocytosis.

Results from P11 *Otof* KOs did not differ much from those of age-matched WT (AP failure rate = $75 \pm 38\%$; range: 0–100%; $n = 11$, two of them failure-free; Fig. 4Ab–Cb and D). The value was statistically indistinguishable from the total failure rate of $96 \pm 5\%$ (Fig. 4D), but the substantial difference of 21% supports the idea of some limitations in the axon terminals (Fig. 4E). Collectively, the results further support our conclusion that MNTB–LSO inputs of WT and *Otof* KOs perform similarly at the time of hearing onset. The two cohorts did not differ significantly in the total failure rate nor the AP failure rate (Fig. 4D; Table 2; *P* values 0.54 and 0.28). The results also demonstrate that a low AP fidelity contributes to a major extent to their relatively low performance at P11 (>3/4).

Table 2. Fidelity of transmission in WT and *Otof* KO at P11 and P38

		Stimulation frequency (Hz)							
		1	2	5	10	20	50	100	200
TotFid s₅₀₋₆₀ (%)	P11	100 ± 0	100 ± 0	91 ± 19	93 ± 18	88 ± 23	28 ± 22	7 ± 7	5 ± 4
	WT	(11)	(11)	(11)	(11)	(11)	(9)	(9)	(9)
	P11	100 ± 0	100 ± 0	81 ± 31	80 ± 32	71 ± 38	12 ± 14	4 ± 5	4 ± 2
	<i>Otof</i> KO	(12)	(12)	(12)	(12)	(12)	(9)	(9)	(8)
P value P11 WT vs. P11 KO		^U	^U	0.85 ^U	0.52	0.64	0.17	0.28	0.26
TotFid s₅₀₋₆₀ (%)	P38	100 ± 0	100 ± 0	100 ± 0	99 ± 3	99 ± 3	90 ± 8	76 ± 21	29 ± 18
	WT	(13)	(13)	(13)	(13)	(12)	(12)	(12)	(12)
	P38	100 ± 0	100 ± 0	83 ± 21	81 ± 18	76 ± 23	53 ± 24	14 ± 12	6 ± 4
	<i>Otof</i> KO	(11)	(11)	(11)	(11)	(11)	(10)	(10)	(9)
P value P38 WT vs. P38 KO		^U	^U	0.81 ^U	0.003	0.004	2.2E-5	1.7E-7	9.9E-4
P value P11 WT vs. P38 WT		^U	^U	0.83 ^U	0.03	0.007	2.4E-9	3.3E-8	3.6E-4
P value P11 WT vs. P38 WT		^U	^U	0.90 ^U	0.87	0.73	3.3E-4	0.04	0.02
P value P11 KO vs. P38 KO		^U	^U	0.83 ^U	0.03	0.007	2.4E-9	3.3E-8	3.6E-4
APFid s₅₀₋₆₀ (%)	P11	100 ± 0	-	-	99 ± 3	-	76 ± 7	34 ± 10	12 ± 6
	WT	(14)			(14)		(14)	(14)	(14)
	P11	100 ± 0	-	-	98 ± 4	-	51 ± 6	25 ± 7	7 ± 7
	<i>Otof</i> KO	(11)			(11)		(11)	(11)	(11)
P value P11 WT vs. P11 KO		1.00 ^U	-	-	0.88 ^U	-	0.17	0.54	0.72 ^U
APFid s₅₀₋₆₀ (%)	P38	100 ± 0	-	-	100 ± 0	-	89 ± 5	80 ± 5	48 ± 9
	WT	(13)			(13)		(13)	(13)	(13)
	P38	100 ± 0	-	-	100 ± 0	-	93 ± 4	71 ± 7	35 ± 9
	<i>Otof</i> KO	(16)			(16)		(16)	(16)	(16)
P value P38 WT vs. P38 KO		1.00 ^U	-	-	1.00 ^U	-	0.53 ^U	0.65 ^U	0.33
P value P11 WT vs. P38 WT		1.00 ^U	-	-	1.00 ^U	-	0.26 ^U	0.003 ^U	0.03 ^U
P value P11 WT vs. P38 WT		1.00 ^U	-	-	0.81 ^U	-	0.003 ^U	0.004	0.01
P value P11 KO vs. P38 KO		1.00 ^U	-	-	0.81 ^U	-	0.003 ^U	0.004	0.01
TotFid vs. APFid	P11	1.00 ^U	-	-	0.006 ^U	-	2.0E-4	0.007	0.72 ^U
	WT								
	P11	1.00 ^U	-	-	0.04 ^U	-	0.02	0.09	0.14
	<i>Otof</i> KO								
	P38	1.00 ^U	-	-	0.1 ^U	-	0.39 ^U	0.03 ^U	0.18
	WT								
P38	1.00 ^U	-	-	2.0E-5 ^U	-	1.0E-4 ^U	1.0E-5	0.003	
<i>Otof</i> KO									
		f_{50Amp} (Hz)	f_{50TotFid} (Hz)	f_{50APFid} (Hz)	f_{50Amp} (Hz)	f_{50TotFid} (Hz)	f_{50APFid} (Hz)		
P11 WT		8	37	78	P11 <i>Otof</i>KO	10	24	53	
P38 WT		9	150	195	P38 <i>Otof</i>KO	10	41	150	

Normalized fidelity values (means ± SD) were determined during s₅₀₋₆₀ of each challenge period (cf. Figs 2–4). Values in brackets depict number of cells. *P* values were determined by a *U* test (superscript U) or an unpaired two-tailed *t* test. AP: action potential; KO: knock-out; WT: wild type.

The situation in young adults was quite different. P38 WT neurons displayed an AP failure rate of $20 \pm 5\%$ during s_{50-60} of 100 Hz challenge (range: 0–97%; $n = 13$, nine of them failure-free; Fig. 4Ac–Cc and D). The value was >3-fold lower than the 66% in P11 WTs (Fig. 4D; Table 2), implying considerable development of the factors determining AP propagation during the first postnatal month (e.g. myelin sheet and nodes of Ranvier). The AP failure rate was statistically indistinguishable from the total failure rate of $24 \pm 21\%$, indicating that synaptic failures play no major role at young adult MNTB–LSO connections. As the synaptic failure rate of P38 WTs appears to be ~7-fold lower than at P11 (Fig. 4E, 4% vs. 27%), we conclude that AP as well as synaptic fidelity improve considerably after hearing onset in WTs, and that

the release and replenishment machineries develop to a level that provides high robustness and indefatigability to neurotransmission.

In deaf P38 *Otof* KOs, a mean AP failure rate of $29 \pm 7\%$ occurred during s_{50-60} of 100 Hz challenge (range: 0–98%; $n = 16$, eight of them failure-free; Fig. 4Ad–Cd and D). The value is >2.5-fold lower than the 75% at P11 (Fig. 4D), implying considerable maturation of AP fidelity despite deafness. Given the high total failure rate of $86 \pm 12\%$ in P38 *Otof* KOs (Fig. 4E), 2/3 of the failures (57% of 86%) appear to be due to deficiencies in the axon terminals. Moreover, the almost 15-fold higher value of 57% compared with 4% in WTs (Fig. 4E) points to the crucial importance of functional otoferlin and acoustic experience for the maturation

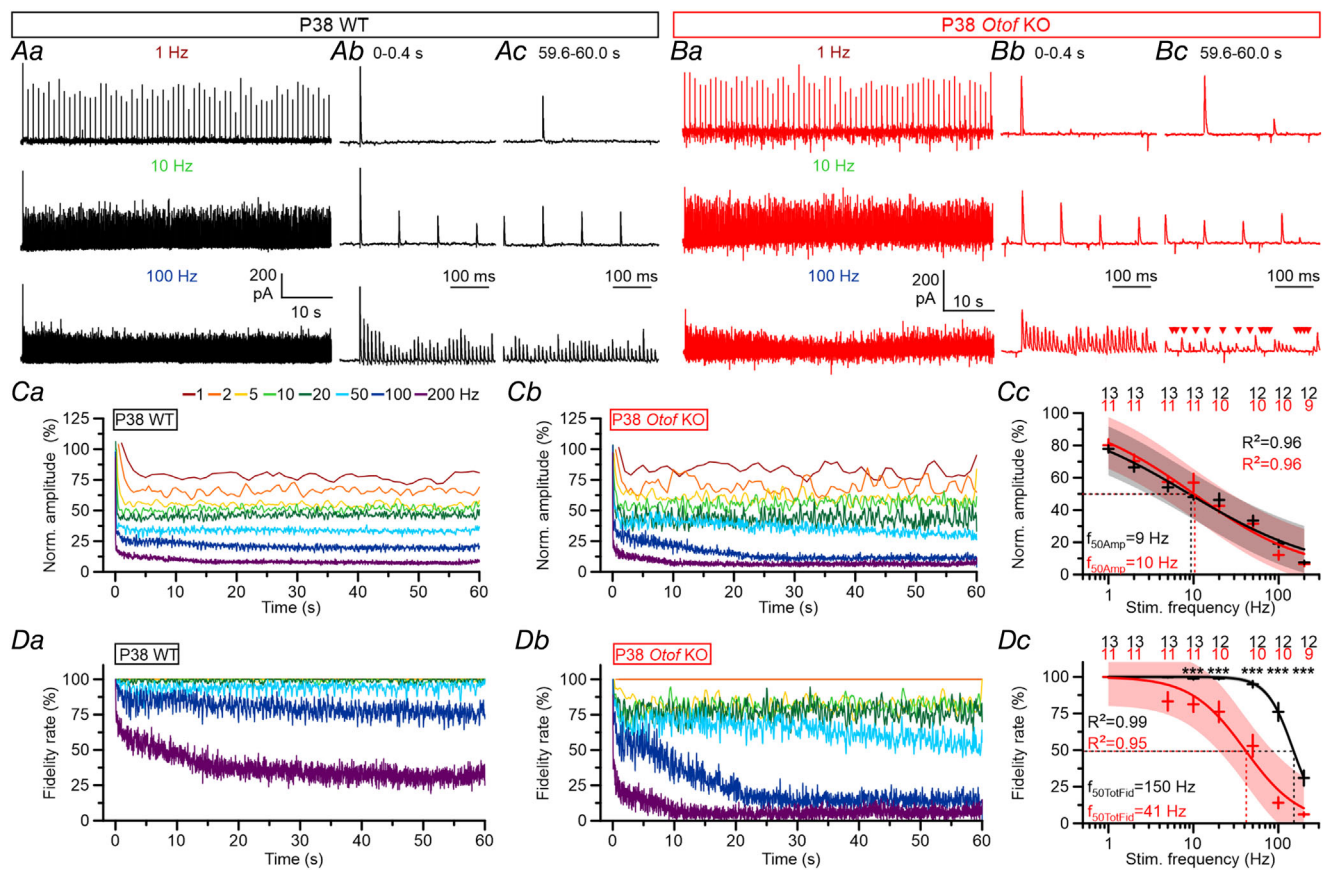


Figure 3. Reduced transmission fidelity in P38 *Otof* KOs

A, B, eIPSCs of a P38 WT (A) and an *Otof* KO neuron (B) during 60 s challenge of single MNTB fibres at 1, 10 and 100 Hz (Aa, Ba) and respective close-ups at the trains' start ($s_{0-0.4}$; Ab, Bb) or end ($s_{59.6-60.0}$; Ac, Bc). Triangles above traces mark synaptic failures. Ca, Cb, time course of mean normalized eIPSC amplitudes in P38 WTs (Ca) and *Otof* KOs (Cb). Cc, frequency dependence of mean normalized eIPSC amplitudes during s_{50-60} . Da–C, as C, but for fidelity. Time courses in Ca–Cb and Da–Db are parabolic weighted moving averages of three (1–2 Hz), five (5–20 Hz), or nine data points (50–200 Hz). Fits in Cc and Dc are sigmoidal regressions. Minimum and maximum values were set to 0 and 1, respectively. Shaded areas depict 95% confidence intervals. f_{50Amp} and $f_{50TotFid}$ values (stippled lines) were determined from sigmoidal regressions. Numbers above plots are number of cells. Statistical comparison of normalized amplitude and fidelity between WTs and *Otof* KOs was done via an unpaired two-tailed *t* test, except for fidelity at 1–5 Hz (U test). Details in Tables 1 and 2. eIPSC: evoked inhibitory post-synaptic currents; KO: knock-out; MNTB: medial nucleus of the trapezoid body; WT: wild type.

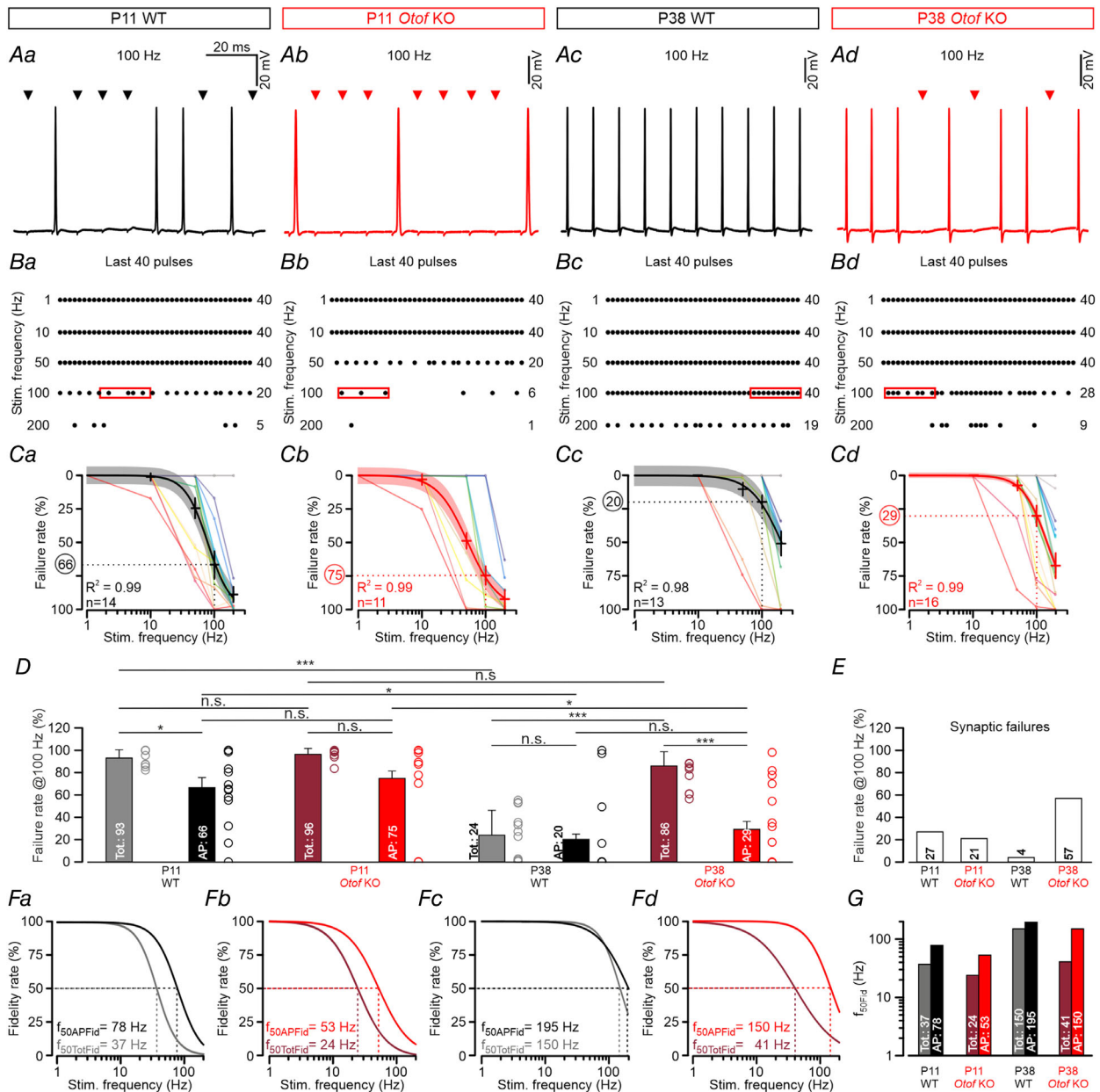


Figure 4. No differences in AP fidelity between P38 WTs and *Otof* KOs

A, original voltage traces from four MNTB neurons of WT and *Otof* KO at P11 (Aa, Ab) and P38 (Ac, Ad). The axon of MNTB neurons was stimulated at the medial border of the LSO to elicit antidromically propagated APs (100 Hz for 60 s). Traces depict 100 ms close-ups during $s_{59.6-60}$. Triangles mark AP failures. **B**, dot plots from the neurons in **A** for five stimulation frequencies (1–200 Hz), illustrating AP fidelity to the last 40 stimulus pulses. Red frames in 100 Hz plots mark the time window shown in **A**. Each dot represents a single AP, and numbers to the right of the plots depict the number of failures at frequencies ≥ 50 Hz. **C**, frequency dependence of AP failure rate. Failure-free AP propagation during s_{50-60} (e.g. 1000 APs at 100 Hz) will result in a failure rate of 0%. Individual single cell data curves are colour-coded, and fits are sigmoidal regressions. Minimum and maximum values were set to 0 and 1, respectively. Shaded areas depict 95% confidence intervals. Stippled lines mark the failure rate at 100 Hz; exact values are provided in circles. **D**, statistical analysis of failure rates during s_{50-60} of 100 Hz challenge (three-way ANOVA and Šidák's correction). **E**, synaptic failure rates calculated from the data depicted in **D** (Synaptic failures = Total failures - AP failures; e.g. 27% = 93% - 66%). **F**, frequency dependence of AP fidelity and total fidelity (cf. panel Ca–d and Fig. 2Cc, Dc). Stippled lines mark $f_{50APFid}$ and $f_{50TotFid}$; exact values are also provided. **G**, direct comparison of f_{50Fid} values (Tot and AP) during s_{50-60} of 100 Hz challenge; exact values are provided in the columns. Notice very similar values for P38 WTs (150 and 195 Hz) and, in contrast, strikingly varying values for P38 KOs (41 and 150 Hz). AP: action potential; KO: knock-out; LSO: lateral superior olive; MNTB: medial nucleus of the trapezoid body; WT: wild type.

of robust release and replenishment machineries after hearing onset.

Figure 4D illustrates another interesting aspect: the AP failure rate declines considerably from P11 to P38 in each genotype (from 66% to 20% in WT, from 75% to 29% in KOs), implying that acoustic experience is not essential to achieving high AP fidelity. Moreover, at each age the AP failure rate is statistically indistinguishable between cohorts, indicating no functional impairment in MNTB axons upon *Otof* loss. Most important for the present study, however, are the differences in the fidelity of SV replenishment and/or SV release. Whereas the participating machineries become normally very resilient and indefatigable after hearing onset, as evidenced by the very low synaptic failure rate in P38 WT, the improvement is lacking in deaf *Otof* KOs (Fig. 4E).

We finally assessed AP fidelity by determining $f_{50\text{APFid}}$ values. At P11, $f_{50\text{APFid}}$ amounted to 78 Hz in WT and 53 Hz in *Otof* KOs (Fig. 4Fa,b). $f_{50\text{TotFid}}$ was about 2-fold lower, namely 37 and 24 Hz (Fig. 4Fa,b and G; see also Fig. 2Da,c), demonstrating a substantial contribution of AP failures to the total transmission behaviour in juveniles. At P38, $f_{50\text{APFid}}$ was 195 Hz in WT vs. 150 Hz in *Otof* KOs (Fig. 4Fc, d and G). Both values were ~2.5-fold higher than at P11 (Fig. 4G), again pointing to hearing-independent improvement of AP generation and conduction properties. Finally, the small 1.3-fold difference between $f_{50\text{APFid}}$ and $f_{50\text{TotFid}}$ in P38 WT, as opposed to a 3.7-fold difference in *Otof* KOs, again supports our conclusion that synaptic failures play no major role in young adults, but they do so upon *Otof* loss-induced deafness (Fig. 4G).

Stable stimulus artefacts and missing correlation between number of preceding AP failures and subsequent eIPSC amplitude

From the above AP fidelity analysis, we exclude differences in excitability as a serious aspect of different transmission behaviour. We further analysed stimulation stability during high-frequency challenge, as unstable stimulus amplitudes may compromise AP generation. We found no evidence for unreliable stimulation conditions, because peak-to-peak stimulus artefacts did not fluctuate over time (not shown). Moreover, there was no (negative) correlation between peak-to-peak stimulus artefacts and the AP failure rate.

A further possibility to distinguish between synaptic depression and reduced excitability is to determine whether there is a (positive) correlation between the number of preceding failures and the amplitude of the subsequent non-failure eIPSC. In the case of synaptic depression, and in contrast to an excitability scenario, such an amplitude should not be especially high. We

determined the distributions of non-failure eIPSC amplitudes during the steady-state phase (s_{50-60}) of 100 Hz challenge at P38 (see Figs 3Ac, Bc and 9Ab for raw traces). WT as well as *Otof* KOs displayed right-skewed (left-leaning) distributions with the maximum in the 40–80 pA bin for each genotype (Fig. 5Aa and Ac). However, the highest eIPSC amplitudes differed considerably (Fig. 5Ab and d; WT: 460 pA, one response; KO: 140 pA, 14 responses). In *Otof* KOs, such eIPSCs of 140 pA were elicited after 0–10 failures (Fig. 5Ad; 14 of 1400 non-failures; median number of preceding failures: 2; range: 0–148). In WT, high amplitudes (≥ 340 pA) occurred after 0–2 failures (Fig. 5b; 27 of 9135 non-failures; median number of preceding failures: 0; range: 0–20). Thus, there was no (positive) correlation between the eIPSC amplitude and the number of preceding failures.

We also checked for reduced excitability by analysing the difference and the ratio of amplitudes from subsequent eIPSCs (i and $i+1$) with and without failures in between. Again, this was done at P38 during s_{50-60} of 100 Hz challenge (Fig. 5Ba–d). In both genotypes, eIPSC_{i+1} did not increase systematically when the number of failures became higher. Even with 10 failures (110 ms gap), eIPSC_{i+1} was similar to eIPSC_i . This implies that within-challenge recovery gaps of 110 ms are too short to enable effective replenishment of empty sites and recovery from depression. A notable difference between genotypes became obvious at ≥ 11 failures (≥ 120 ms gaps). Here, eIPSC_{i+1} in WT was ~60 pA or ~2-fold higher than eIPSC_i (Fig. 5Ba–d), implying effective replenishment if within-challenge recovery gaps are ≥ 120 ms. This time window relates to an effective stimulation frequency of ~8 Hz. In contrast to WT, within-challenge recovery was absent in *Otof* KOs (Fig. 5Bc and d). Together, the results argue against excitability differences between WT and *Otof* KOs as an important factor in explaining the difference in the ability to fire APs at high rate.

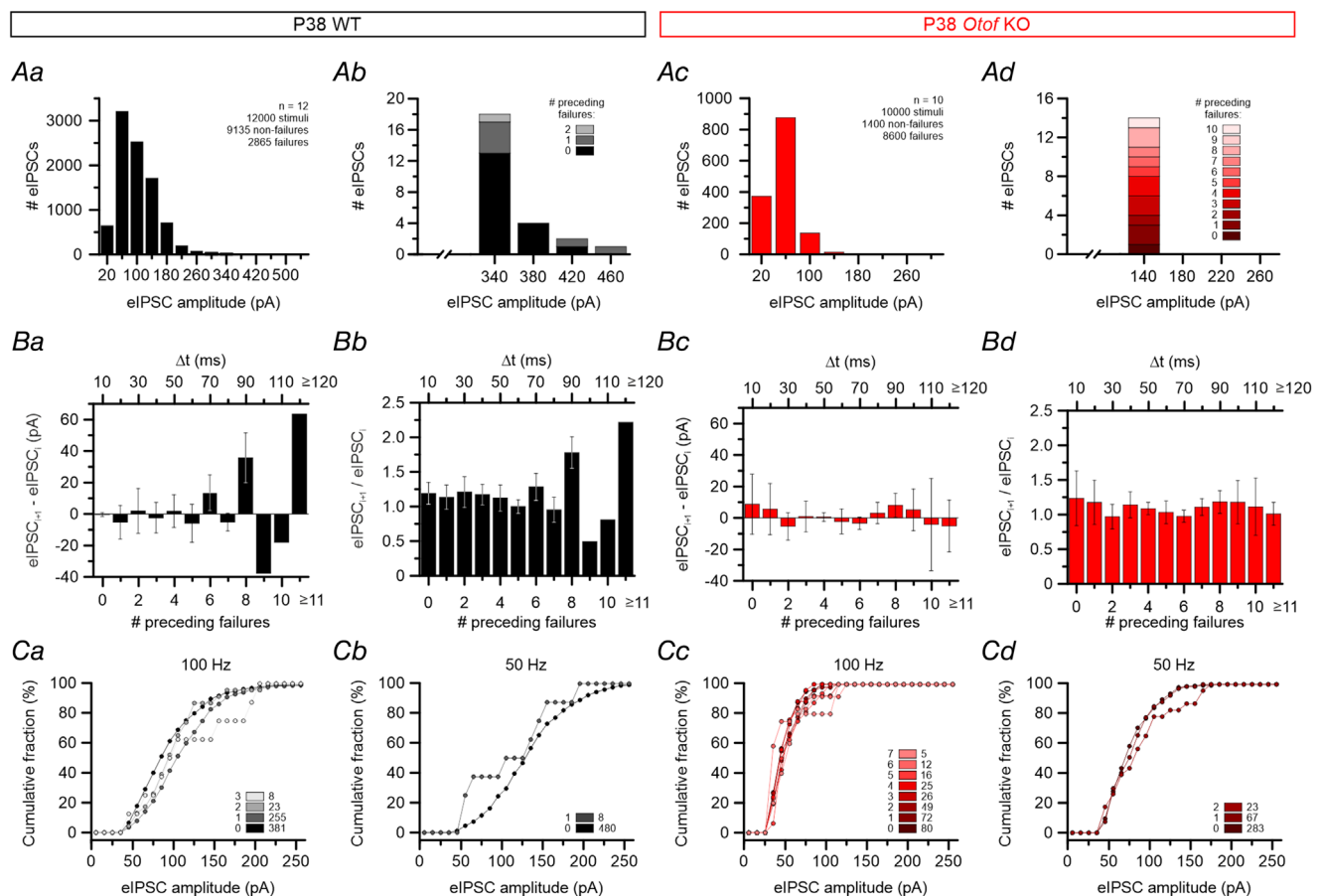
Since pooled sample data fail to reveal the characteristics of individual measurements, we next analysed the performance of individual neurons by generating cumulative plots of eIPSC amplitudes obtained at various numbers of preceding failures (Fig. 5C). At P38, when failure rates differ drastically between WT and *Otof* KOs (cf. Fig. 4D and E), these plots displayed no systematic right-shift when the number of preceding failures increased and more time was available for replenishment, neither during the 100 Hz nor the 50 Hz train (Fig. 5Ca–d). Instead they consistently displayed mean eIPSC amplitudes of ~80 pA in the WT and ~50 pA in the KO, confirming weak replenishment in the tens of milliseconds range. In contrast, the two inputs recuperated substantially during the first 2 s of the 1 Hz recovery period (eIPSC in WT: 219 pA; in KO: 116 pA),

demonstrating robust replenishment capacity in the second range. Recovery will be addressed in detail in the next section.

Normal recovery from synaptic attenuation in *Otof* KOs

The above results, including those from the antidromic stimulation experiments, imply that the low total fidelity in P38 *Otof* KOs is caused predominantly by synaptic failures (Fig. 4D and F; see also Fig. 3D). To assess whether KOs may display impaired recovery from synaptic

attenuation, we analysed single fibre eIPSCs during a 1 Hz for 60 s recovery period after each challenge period. Example current traces for P11 WT and *Otof* KOs after 100 Hz challenge are shown in Fig. 6A. Mean recovery time courses were unaltered between genotypes, reaching steady-state levels of $\sim 80\%$, independent of the preceding challenge frequency (s₁₁₀₋₁₂₀; Fig. 6Ba and b, Table 3). At P38, steady-state recovery was also indistinguishable between genotypes (Fig. 6C and D, Table 3). Steady-state levels amounted again to $\sim 80\%$, independent of challenge frequency, genotype or age (Fig. 6E, Table 3). eIPSCs did not recover to 100%, because 1 Hz stimulation already led



to a slight synaptic depression (Figs 2C and 3C; Krächan et al., 2017; Kramer et al., 2014). Notably, introducing a 10 s pause between recovery and the subsequent challenge period did result in ~100% recovery (*cf.* starting values of challenge periods in Figs 2C and 3C). Taken together,

Otof KOs display normal recovery behaviour at both ages. Therefore, we conclude that the reduced fidelity at P38 cannot be explained by insufficient recovery capability *per se*. However, rapid within-challenge recovery, i.e. recovery within the short 10 ms windows during 100 Hz challenge,

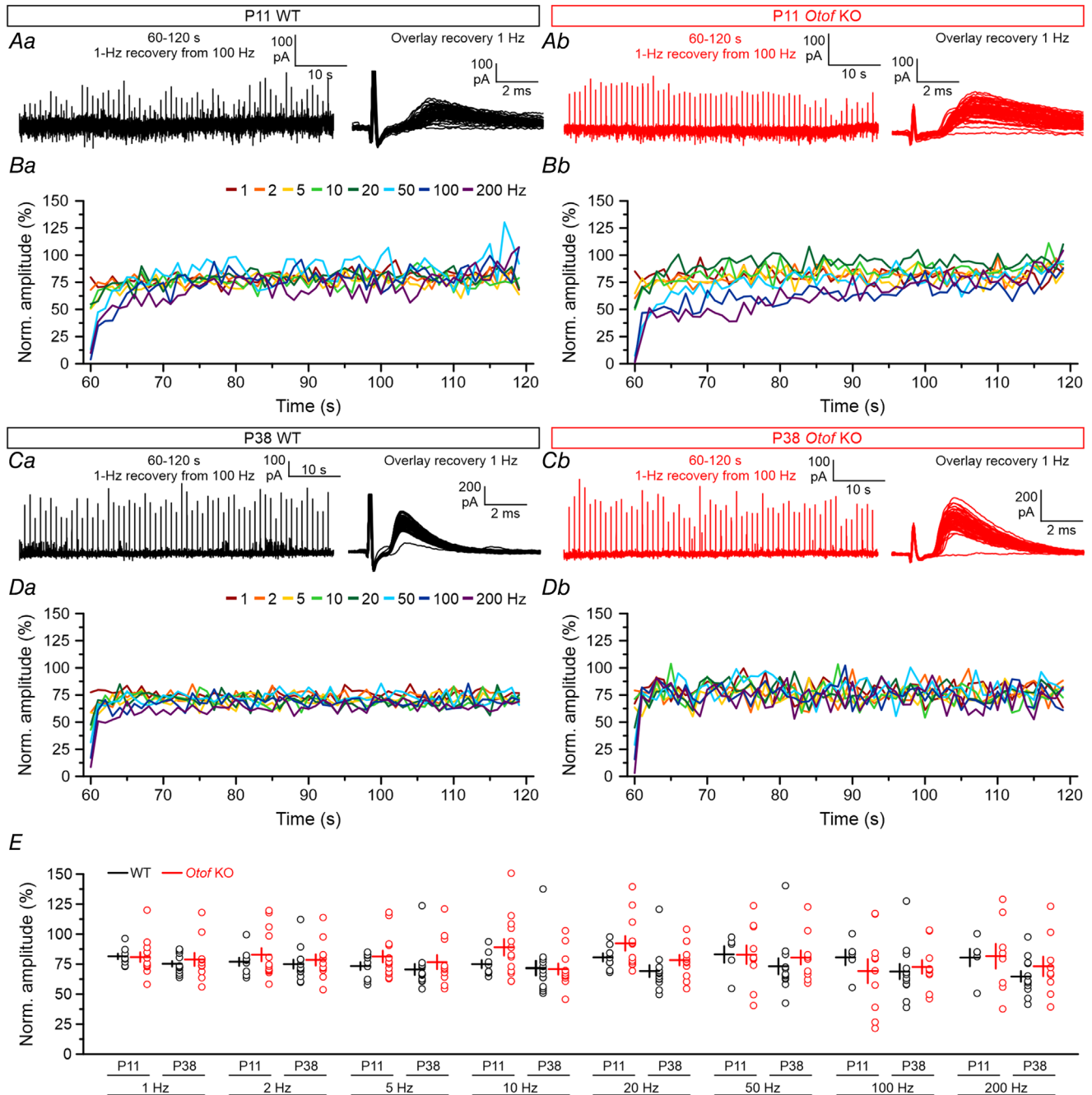


Figure 6. Normal recovery from synaptic attenuation in *Otof* KOs
 A, eIPSCs of a P11 WT (Aa) and an *Otof* KO neuron (Ab) during 1 Hz for 60 s recovery following 100 Hz challenge. Right side in Aa and Ab shows eIPSC overlays at higher temporal resolution. B, time course of mean normalized eIPSC amplitudes during recovery periods in P11 WTs (Ba) and *Otof* KOs (Bb). C, D, as A–B, but at P38. E, mean normalized amplitudes during s_{110–120} of the recovery periods. Statistical comparison of normalized amplitudes between WTs and *Otof* KOs at both ages was done via an unpaired *t* test. Details in Table 3. eIPSC: evoked inhibitory post-synaptic current; KO: knock-out; WT: wild type.

Table 3. Recovery in WT and *Otof* KOs at P11 and P38

		Stimulation frequency (Hz)							
		1	2	5	10	20	50	100	200
eIPSC amplitude $s_{110-120}$ (%)	P11	82 ± 7	77 ± 10	73 ± 10	75 ± 9	81 ± 10	83 ± 16	81 ± 14	80 ± 16
	WT	(9)	(9)	(9)	(8)	(8)	(5)	(5)	(5)
	P11 <i>Otof</i> KO	81 ± 14 (13)	83 ± 20 (13)	81 ± 17 (13)	89 ± 25 (13)	92 ± 21 (12)	83 ± 24 (10)	69 ± 32 (10)	82 ± 29 (8)
P value		0.91	0.44	0.25	0.13	0.12	0.99	0.49	0.94
eIPSC amplitude $s_{110-120}$ (%)	P38	75 ± 8	75 ± 13	71 ± 16	72 ± 22	69 ± 17	73 ± 23	69 ± 22	65 ± 15
	WT	(13)	(13)	(13)	(13)	(12)	(12)	(12)	(12)
	P38 <i>Otof</i> KO	79 ± 17 (10)	79 ± 16 (11)	77 ± 19 (11)	71 ± 15 (11)	78 ± 14 (11)	81 ± 18 (10)	73 ± 18 (10)	73 ± 24 (9)
P value		0.53	0.59	0.43	0.32	0.03	0.33	0.12	0.37

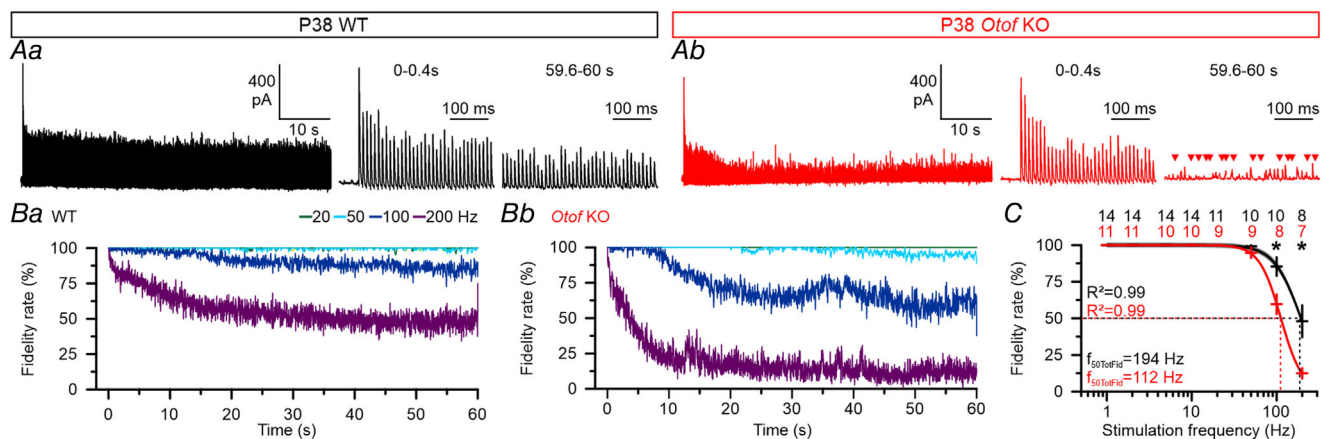
Normalized amplitude values (means ± SD) were determined during $s_{110-120}$ of the recovery period (cf. Fig. 6). 100% represents the baseline value. Values in brackets depict number of cells. *P* values were determined by a *t* test. eIPSC: evoked inhibitory post-synaptic current; KO: knock-out; WT: wild type.

appears to be drastically impaired upon hearing loss (Fig. 4D).

Fidelity analysis during single fibre stimulations is not biased by low eIPSC-to-noise ratios

eIPSC peak amplitudes ≤ 1.5 times q (33 pA with $q = 22$ pA) were considered a failure in this study. Our threshold was ~ 2 -fold higher than the peak-to-peak noise level of ~ 15 pA. Low eIPSC-to-noise ratios may cause detection limits and thus compromise fidelity assessment in that small eIPSCs remain undetected. To check the robustness of our fidelity analysis, we performed

maximal stimulation experiments at P38 and determined the fidelity with the same criteria used for minimal stimulation. Despite pronounced synaptic attenuation during s_{50-60} , eIPSC peak amplitudes were large enough to be clearly distinguishable from noise (Fig. 7Aa and b). Consequently, maximal stimulation yielded higher eIPSC-to-noise ratios than minimal stimulation. Even at higher eIPSC-to-noise ratios, *Otof* KOs showed more synaptic failures than WTs, resulting in 40% and 75% lower fidelity at 100 and 200 Hz, respectively (Fig. 7B and C; WT 100 Hz: $86 \pm 20\%$, $n = 10$; *Otof* KO 100 Hz: $60 \pm 19\%$, $n = 8$, $P = 0.02$; WT 200 Hz: $48 \pm 31\%$, $n = 8$; *Otof* KO 200 Hz: $12 \pm 9\%$, $n = 7$, $P = 0.02$, unpaired

**Figure 7. Reduced total fidelity in P38 *Otof* KO neurons during maximal stimulation**

A, eIPSCs of a P38 WT (Aa) and an *Otof* KO neuron (Ab) during 100 Hz for 60 s challenge as well as close-ups at the trains' start ($s_{0-0.4}$) or end ($s_{59.6-60}$). Triangles in Ab mark synaptic failures. B, time course of mean total fidelity in WTs (Ba) and *Otof* KO neurons (Bb). 50–200 Hz curves are parabolic moving averages over nine data points. Curves for 1–10 Hz are at 100% (no failures) and are covered by the 20 Hz trace. C, mean total fidelity during s_{50-60} and fits via sigmoidal regression (as in Figs 2 and 3). Numbers above plot are cell numbers. Statistical comparison of total fidelity between WTs and *Otof* KO neurons was done via an unpaired two-tailed *t* test. eIPSC: evoked inhibitory post-synaptic current; KO: knock-out; WT: wild type.

t tests). In accordance with these findings, $f_{50\text{TotFid}}$ was $\sim 40\%$ lower in *Otof* KOs (112 vs. 194 Hz; Fig. 7C).

Taken together, the reduced fidelity in *Otof* KOs during both minimal and maximal stimulation demonstrates the robustness of our threshold-based fidelity analysis, even when eIPSC-to-noise ratios are low. Furthermore, the higher number of converging fibres in *Otof* KOs (6 vs. 4; cf. Fig. 1Aa, and Müller et al., 2019) does not rescue the fidelity.

Normal size of the readily releasable pool in *Otof* KOs

We next investigated whether a reduced RRP size and/or a higher initial P_v might contribute to the reduced fidelity seen in P38 *Otof* KOs. Furthermore, we assessed RRP development using the method of Elmqvist & Quastel (1965). We challenged the inputs in 100 Hz for 1 s trains (maximal stimulation; 20 repeats) at both P11 and P38 (Fig. 8A). eIPSC depression was similar between WT and *Otof* KOs in terms of absolute and normalized amplitudes and in terms of SVs (Fig. 8B). At both ages, the combined RRP across all convergent MNTB fibres was statistically indistinguishable between *Otof* KOs and WT (Fig. 8Ca, b and Da; P11 WT: 561 ± 271 SVs, $n = 15$, P11 *Otof* KO: 541 ± 224 SVs, $n = 7$, $P = 0.87$; P38 WT: 321 ± 148 SVs, $n = 12$, P38 *Otof* KO: 345 ± 379 SVs, $n = 8$, $P = 0.88$, unpaired *t* tests). During post-hearing development, RRP decreased by $>40\%$ in WT (321/561, $P = 0.01$, unpaired *t* test). We obtained a similar, yet insignificant decrease in *Otof* KOs (345/541, $P = 0.27$, unpaired *t* test).

The initial P_v was normal in *Otof* KOs at both ages (Fig. 8Db; P11 WT: 0.13 ± 0.05 , $n = 15$; P11 *Otof* KO: 0.12 ± 0.04 , $n = 7$; $P = 0.88$; P38 WT: 0.17 ± 0.06 , $n = 12$; P38 *Otof* KO: 0.18 ± 0.07 , $n = 8$; $P = 0.89$, unpaired *t* test). Moreover, neither genotype displayed an age-related change (WT: $P = 0.04$; *Otof* KO: $P = 0.08$, unpaired *t* tests, Šidák's correction). Notably, P_v is the combined release probability of several fibres here because of maximal stimulation. Of course, P_v values of individual fibres fluctuate around this mean value. Taken together, because of the normal initial RRP and normal initial P_v in *Otof* KOs, both parameters do not contribute to the reduced fidelity in P38 mutants. We reason that the reduced fidelity may be due to release deficits which become manifest during sustained stimulation. A lower replenishment capacity may be one cause.

No developmental increase in replenishment capacity in *Otof* KOs

To determine the replenishment capacity, we calculated the cumulative number of released SVs for each genotype (minimal stimulation, 100 Hz for 60 s). eIPSC analysis at P11 confirmed that SVs are primarily released at the start

of the train in both genotypes (Fig. 9Aa, left half). At the train's end, the number of SVs released per stimulus was low in either genotype, as evidenced by an excessively high number of failures (Fig. 9Aa right half; Figs 2 and 3). The same scenario was evident in P38 *Otof* KOs (Fig. 9Ab). In contrast, SV release persisted in P38 WT, and failures were therefore rare, even at the train's end (Figs 9Ab and 3Ac). Consequently, the cumulative number of released SVs amounted to $\sim 24,000$ SVs in P38 WT, a ~ 6 -fold higher value than in P11 WT (4000 SVs), ~ 8 -fold higher than in P11 *Otof* KOs (3000 SVs), and ~ 4 -fold higher in P38 *Otof* KOs (6000 SVs; Fig. 9B). To determine the replenishment capacity during s_{50-60} , we linearly fitted the last 10 s of the cumulative SV release and determined the slope as a proxy for the RR (Fig. 9Ba and b). $RR_{s_{50-60}}$ was similar between WT and *Otof* KOs at P11 (Fig. 9Ba and C; WT: 44 ± 26 SVs/s, $n = 7$; *Otof* KO: 33 ± 27 SVs/s, $n = 9$; $P = 0.45$, unpaired *t* test). WT displayed an ~ 8 -fold higher RR at P38 than at P11 (Fig. 9C; 348 ± 160 SVs/s, $n = 12$; $P = 8.8E-5$, unpaired *t* test). By contrast, RR of *Otof* KOs did not change significantly with age (Fig. 9C; P38 *Otof* KOs: 70 ± 34 SVs/s; $n = 9$; $P = 0.03$, unpaired *t* test). In line with this, the RR in P38 *Otof* KOs was 80% lower than in age-matched WT ($P = 0.0002$, unpaired *t* test).

There is a caveat to the analysis performed in Fig. 9A–C because the obtained RR values do not consider the contribution of AP failures and detection failures. Such failures amounted to 75% in P11 *Otof* KOs and to 29% in P38 *Otof* KOs during s_{50-60} of 100 Hz challenge (cf. Fig. 4D), thereby resulting in lower effective stimulation frequencies and thus potentially in erroneous, overestimated RR values. In the section 'Computational modelling reveals reduced RR per site in *Otof* KOs', below, we will elaborate this concern and refute it.

Previously, we described a difference in single fibre quantal content between WT and *Otof* KOs (Müller et al., 2019). To control for this difference, we also compared the normalized time courses of cumulatively released SVs (maximum = 100%; Fig. 9Da and b). WT and *Otof* KO time courses overlapped considerably at P11, confirming the similarity in incremental SV release. By contrast, P38 *Otof* KOs revealed a reduced slope during s_{50-60} , thus manifesting the reduced incremental SV release compared with WT (Fig. 9Db). Remarkably, the reduced slope became manifested already after ~ 20 s. As RR and fidelity were high in P38 WT, we checked for a potential correlation between the two parameters. To do so, we plotted RR against fidelity for all four cohorts (Fig. 9Ea). We found a sigmoidal relationship, revealing that 50% fidelity is reached at a RR of ~ 165 SVs/s, whereas 100% fidelity is acquired at RRs > 500 SVs/s (Fig. 9Eb).

Taken together, the RR of single MNTB-LSO inputs increase ~ 8 -fold from P11 until P38, which explains the high neurotransmission fidelity during sustained

high-frequency stimulation at P38. Because deaf *Otof* KOs lack a high RR, the formation of a robust replenishment capacity appears to depend on acoustic experience.

Computational modelling reveals reduced RR per site in P38 *Otof* KOs

To further validate our empirical data, we applied computational modelling and determined RR throughout

challenge and recovery (100 Hz for 60 s and 1 Hz for 60 s, respectively). Moreover, we assessed RR for single sites (*Methods*, equation 3). The model captured the experimental data very well for each cohort (Fig. 10A). In P38 WT, RR peaked at ~ 620 SVs/s (Fig. 10Ba). Corresponding values in the other three cohorts were less than half, yet similar for inter-cohort comparison (P11 WT: ~ 260 SVs/s; P11 *Otof* KO: ~ 280 SVs/s; P38 *Otof* KO: ~ 270 SVs/s). Each cohort reached a steady-state RR after

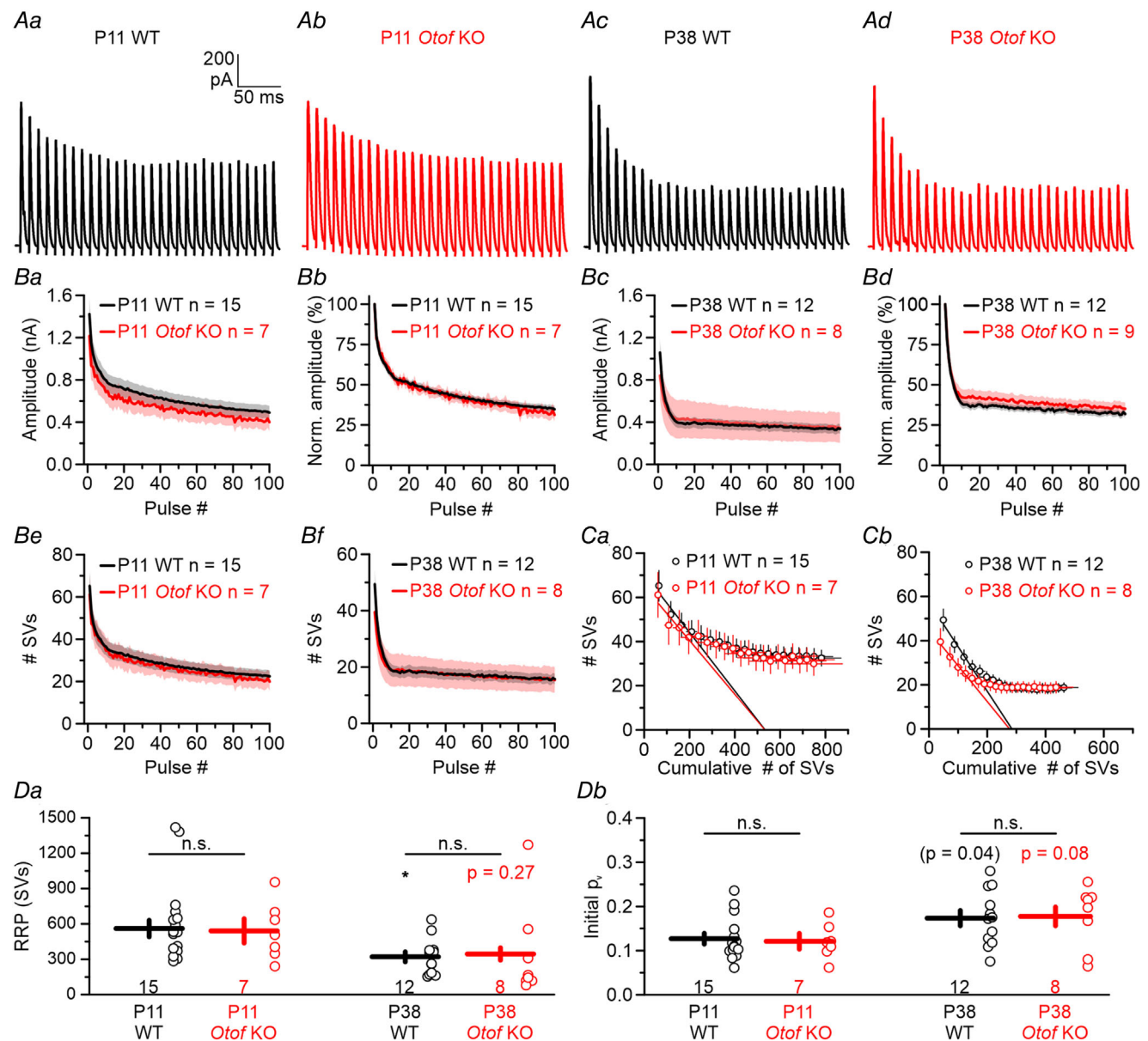


Figure 8. Normal RRP size in *Otof* KOs

A, current traces depicting eIPSC₁₋₃₀ during 100 Hz for 1 s maximal stimulation in a P11 WT (Aa), a P11 *Otof* KO (Ab), a P38 WT (Ac) and a P38 *Otof* KO neuron (Ad). B, time course of absolute eIPSC amplitudes (Ba, Bc), normalized amplitudes (Bb, Bd) and SVs (Be, Bf). C, RRP size at P11 (Ca) and P38 (Cb) determined via the Elmqvist & Quastel method. D, statistics for RRP size (Da) and initial p_v (Db). Numbers in plots are number of cells. Statistical comparison between WTs and *Otof* KOs was done via an unpaired *t* test. eIPSC: evoked inhibitory post-synaptic current; KO: knock-out; RRP: readily releasable pool; SV: synaptic vesicle; WT: wild type.

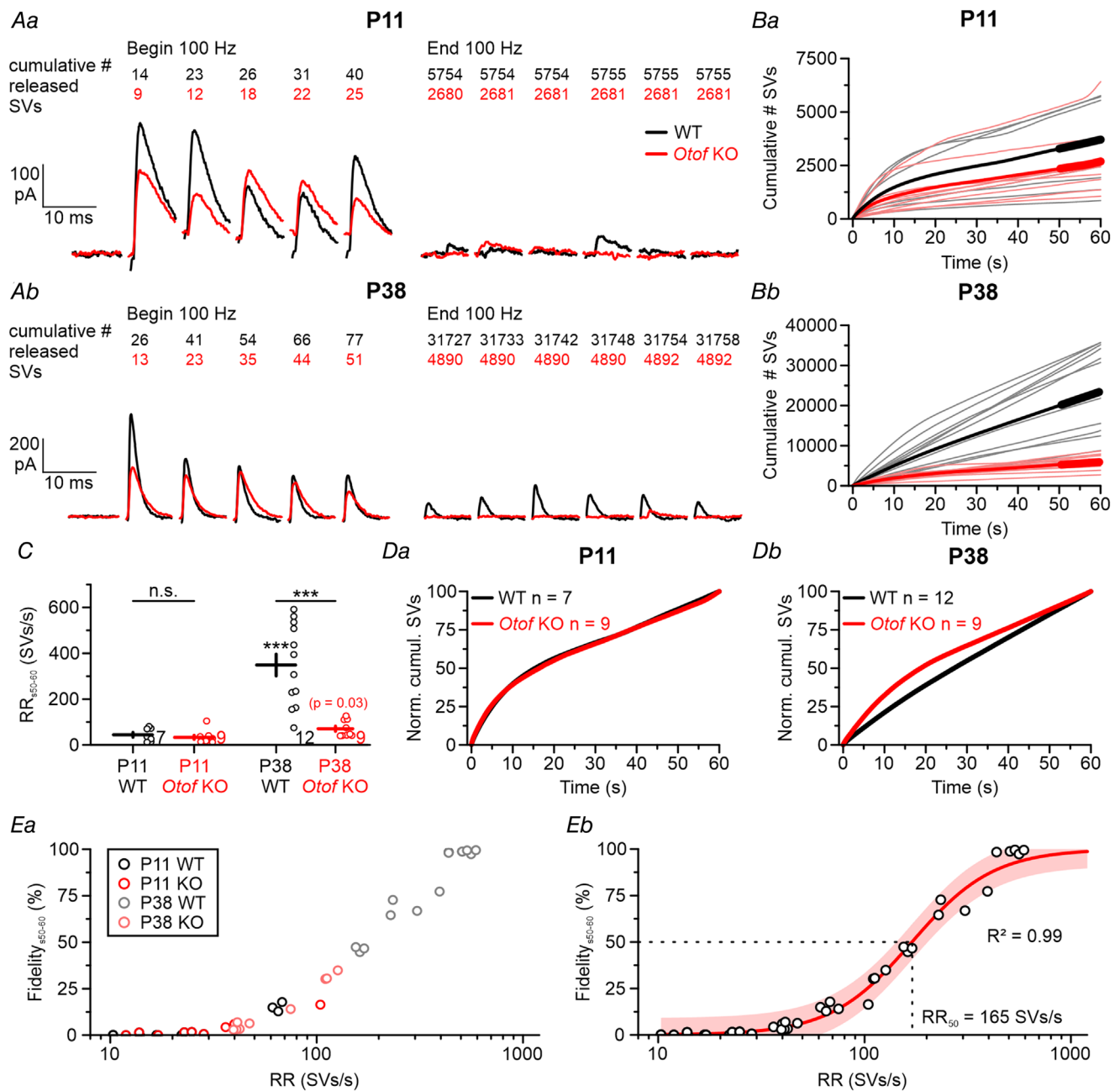


Figure 9. No developmental increase in replenishment capacity in *Otof* KOs

Aa, single fibre eIPSCs of a P11 WT (black) and a P11 *Otof* KO neuron (red) at the start and end of a 100 Hz for 60 s train. Numbers above eIPSCs indicate the cumulative number of released SVs. Ab, same as Aa, but at P38. B, time course of cumulatively released SVs in WT and *Otof* KOs at P11 (Ba) and P38 (Bb). Thin lines depict single recordings, thicker lines are mean values, and thickest lines (s₅₀₋₆₀) mark period in which RR was quantified. C, statistics for RR. Numbers in plot are number of cells. Statistical comparison between WT and *Otof* KOs was done via an unpaired *t* test. D, normalized time course of cumulatively released SVs (maximum = 100%). E, total fidelity as a function of the RR (period analysed: s₅₀₋₆₀). Data points were colour-coded for groups (Ea) and described with a sigmoidal fit (Eb, red line). Shaded area is 95% confidence interval. eIPSC: evoked inhibitory post-synaptic currents; KO: knock-out; RR: replenishment rate; SV: synaptic vesicle; WT: wild type.

~20 s that amounted to 33 SVs/s in P11 WT, 30 SVs/s in P11 *Otof* KO, 356 SVs/s in P38 WT, and 66 SVs/s in P38 *Otof* KO (s_{50-60} ; Fig. 10Ba). Thus, steady-state RRs increased ~11-fold in WT, but only ~2-fold in *Otof* KO between P11 and P38. These model-based numbers are close to the proxies from the experimental data (8-fold and 2-fold, respectively; cf. Fig. 9C). When normalized to the maximum rate, RR during s_{50-60} dropped to ~10% in P11 WT and P11 *Otof* KO (Fig. 10Bb). RR in P38 *Otof* KO declined to ~25%, whereas P38 WT maintained an RR of ~60% throughout the train. As the quantal content differed up to ~3-fold across cohorts (Fig. 10A), we normalized the RR to the initial RRP for each cohort (initial RRP size determined by the model). In P11 WT and *Otof* KO, the RRP became replenished 1-fold/s during s_{50-60} (Fig. 10Ca). Corresponding values were

~1.5-fold/s in P38 *Otof* KO and ~4-fold/s in P38 WT. Pooling challenge and recovery trains, the cumulative replenishment of the RRP was ~70-fold in P11 WT, ~61-fold in P11 *Otof* KO, ~240-fold in P38 WT, and ~130-fold in P38 *Otof* KO (Fig. 10Cb). When related to a single site, RR amounted to ~0.8 SVs/s in P11 WT, ~0.7 SVs/s in P11 *Otof* KO, ~4.5 SVs/s in P38 WT, and ~1.5 SVs/s in P38 *Otof* KO (s_{50-60} ; Fig. 10Da). These values correspond to ~10% of the maximal RR per site in P11 WT, ~10% in P11 *Otof* KO, ~50% in P38 WT, and ~20% in P38 *Otof* KO (Fig. 10Db). About 95% of the sites were empty during steady-state in P11 WT, ~95% in P11 *Otof* KO, ~80% in P38 WT, and ~90% in P38 *Otof* KO (Fig. 10Ea). Although these values appear to be quite similar, the P38 WT cohort is clearly distinct. Finally, the reoccupation time for a site was ~1.23 s in P11 WT,

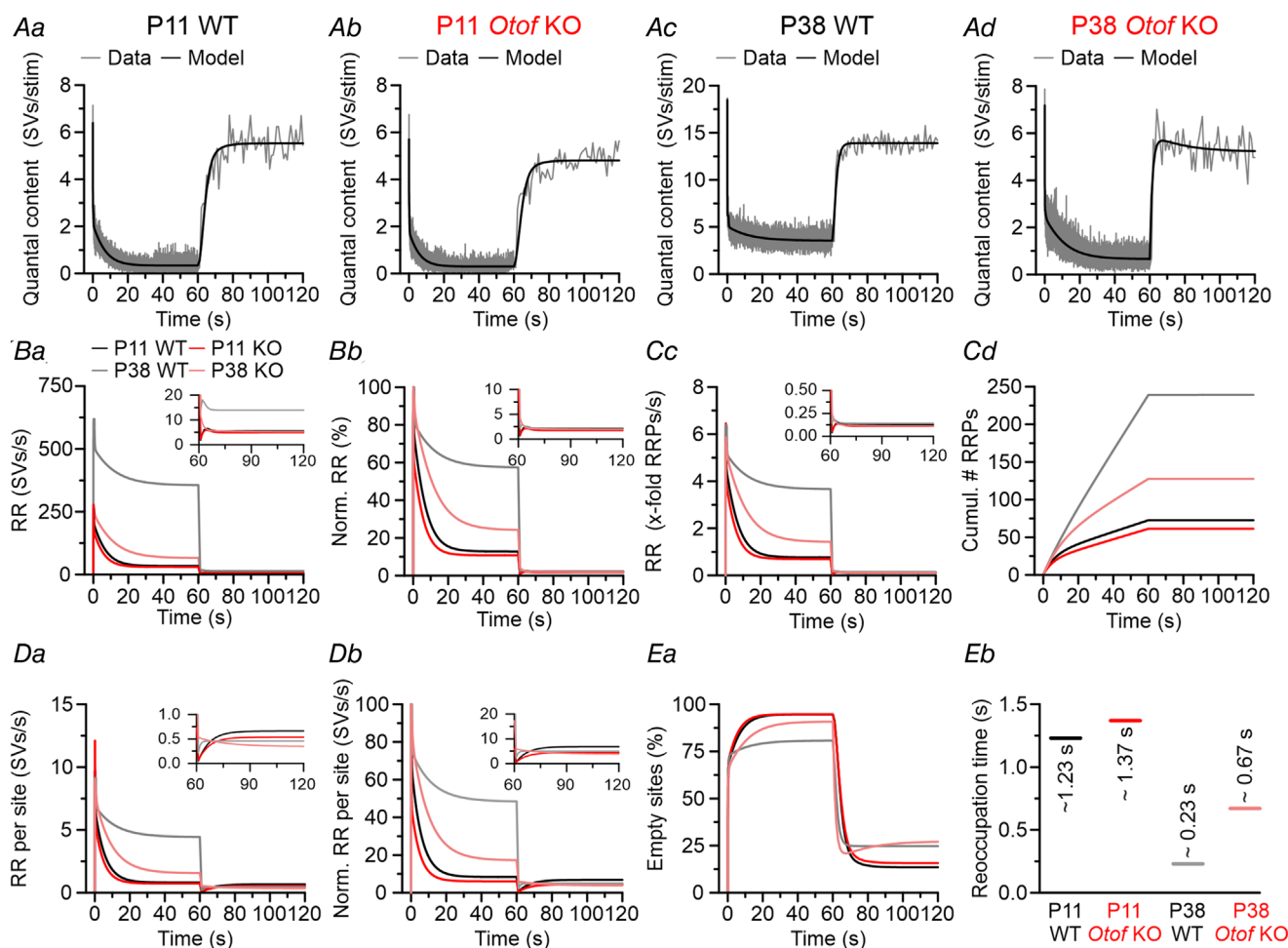


Figure 10. Computational modelling reveals a reduced RR per site in *Otof* KO

A, time course of quantal content during 100 Hz for 60 s challenge and subsequent recovery (1 Hz) for WT and *Otof* KO at P11 and P38. B, time course of RR (Ba) and normalized RR (Bb). C, time course of RR in x-fold RRP (Ca) and normalized RR per site (Cb). D, time course of RR per site (Da) and normalized RR per site (Db). Insets in B–D are y-axis-expanded close-ups of the recovery period. Ea, time course of empty sites, normalized to 100%. Eb, time for reoccupying an empty site with a new SV (mean from s_{50-60}). Notice: RR in Ba quantifies net replenishment, whereas RR per site in Da quantifies replenishment at a single empty site. KO: knock-out; RR: replenishment rate; RRP: readily releasable pool; SV: synaptic vesicle; WT: wild type.

~1.37 s in P11 *Otof* KOs, ~0.23 s in P38 WTs, and 0.67 s in P38 *Otof* KOs (Fig. 10*Eb*).

AP failures affect SV release only mildly during ongoing high-frequency stimulation

The above results on RR values (Figs 9 and 10*B–D*) neglect the contribution of AP failures. Such failures became particularly frequent at P11 during ongoing

100 Hz challenge (Fig. 4). They result in an increased replenishment time (multiples of 10 ms), which in turn increases the N_{RRP} and ultimately leads to a higher quantal content. To address the issue and to quantify the effect on the quantal content, we added a probabilistic component to equation (2). This component implements random AP failures, therewith creating a realistic scenario. We focused on s_{50-60} of the 100 Hz trains and modelled the time course of SV release for each cohort (Fig. 11*A–C*). Insets

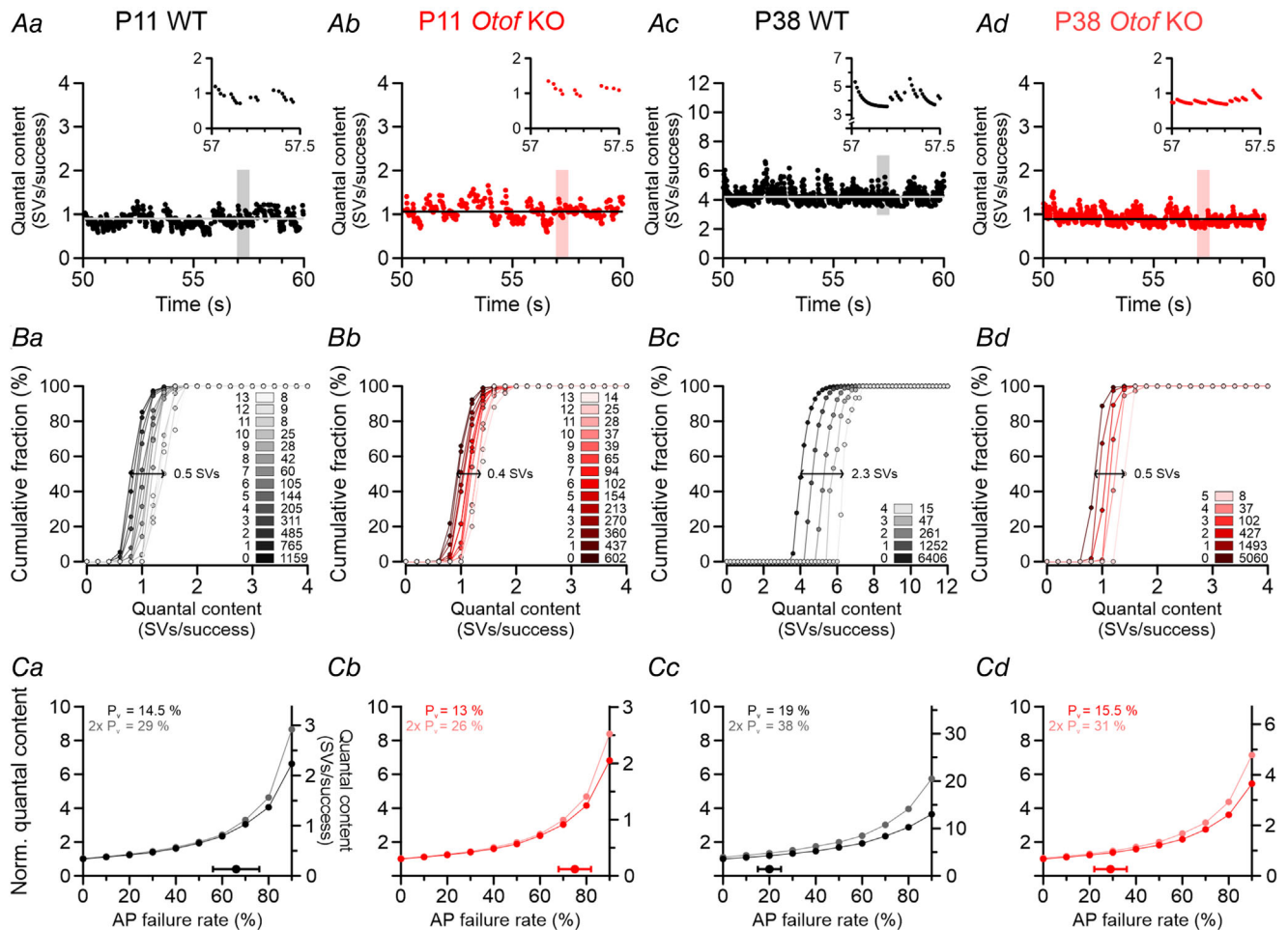


Figure 11. High AP failure rates during ongoing high-frequency stimulation barely affect SV release
 A, time course of quantal content during s_{50-60} of 100 Hz stimulation for WT and *Otof* KO at P11 and P38. Data were calculated via a probabilistic model (see *Methods*) with the following underlying values (Aa–Ad): AP failure rate 66, 75, 20, 29%; P_v 14.5, 13, 19, 15.5%; RR per site 0.8, 0.7, 4.5, 1.6 SVs/s. Note different y-axes for P38 WT. Horizontal lines depict mean quantal content. Shaded areas are $s_{57-57.5}$ periods magnified in insets. B, cumulative fraction of quantal content, based on the computational modelling (10 repeats) in panel A (compare with experimental data in Fig. 5C). Numbers to the left of colour-coded columns depict number of preceding AP failures, whereas numbers to the right depict number of events. The mean ‘recovery gain’ from 0 failures to the maximal number of failures is provided in the panels (e.g. 0.5 SVs in A, upon occurrence of 13 subsequent AP failures (relating to a replenishment time of 140 ms). C, computational modelling of the mean quantal content during s_{50-60} . The AP failure rate was chosen arbitrarily in a broad range from 0 to 90%. The empirical AP failure rate (mean \pm SD) is shown for orientation (cf. Fig. 4D). To demonstrate the effect of P_v , each panel depicts two curves. Normalized values are depicted by the y-axis on the left, absolute values by the y-axis on the right. A supplementary document ‘Interactive modelling of quantal content.xlsm’ allows an interactive view of the scenario and adjustment of the parameters AP failure rate, P_v and RR per site. AP: action potential; KO: knock-out; RR: replenishment rate; SV: synaptic vesicle; WT: wild type.

show 500 ms close-ups of $s_{57-57.5}$ and illustrate exponential depression as well as replenishment for various numbers of AP failures (best seen at P38 WT). Analysis of the s_{50-60} period revealed steady-state levels for the quantal content in each cohort (average for P11 WT: 0.9 SVs/success; P11 *Otof*KO: 1.1; P38 WT: 4.2; P38 KO: 0.9; mean in each case) and relatively little variability after the occurrence of AP failures. We next modelled the performance of each cohort by generating cumulative plots of the quantal content, like for the analysis of experimental data in Fig. 5C. These plots contain curves obtained after various numbers of preceding AP failures (Fig. 11B). At P11, the curves revealed merely a small right-shift of the mean quantal content, mounting to ≤ 0.5 SVs, even with 13 AP failures, which relate to 140 ms replenishment time (Fig. 11Ca,b). This small 'recovery gain' was also seen at P38 for the KOs (Fig. 11Cc). Only the P38 WTs displayed a right-shift of 2.3 SVs with 4 AP failures (= 50 ms replenishment time; Fig. 11Cd). Whereas the P38 WTs showed a systematic recovery gain (~ 0.6 SVs for each 10 ms period), the other three cohorts did not.

We further modelled the dependence of SV release on the AP failure rate by changing this value from 0% to 90% (Fig. 11Ca–d). The computational results revealed relatively flat curves for the quantal content over a broad AP failure range and a >4 -fold increase only for failure rates $>80\%$. In a final step, we increased P_v 2-fold and found almost no effect (Fig. 11Ca–d). Taken together, 50–60 s into ongoing high-frequency stimulation, SV release appears to be quite independent of the number of AP failures and the release probability. SV release in the steady-state phase is therefore determined merely by the RR, in accordance with previous modelling observations (Neher, 2017).

Collectively, computational modelling confirmed our empirical data and revealed a multi-fold higher RR per site in P38 WTs than in the three other cohorts. The high RR in P38 WTs appears to form the basis for robust and high-fidelity neurotransmission during sustained high-frequency stimulation. Our modelling results further suggest an increase in RR for *Otof* KOs between P11 and P38, potentially arguing for an activity-independent, hard-wired mechanism or a compensatory mechanism. Nevertheless, even with such a mechanism, acoustic experience is the main contributor for the increase in RR and for the normal development of synaptic performance.

Normal maturation of neurotransmission latency in *Otof* KOs (low-frequency stimulation)

Prominent features of auditory brainstem synapses are a short latency and a high temporal precision (Ford et al., 2015; Kandler & Friauf, 1995; Krächan et al.,

2017; Taschenberger & von Gersdorff, 2000). The latency mainly depends on the axonal conductance velocity, the vesicular release synchrony, and the neurotransmitter receptor kinetics (Magnusson et al., 2005; Miki et al., 2018; Taschenberger & von Gersdorff, 2000; Turecek & Regehr, 2019). We recently showed that both release synchrony and receptor kinetics accelerate during development in WTs and *Otof* KOs, suggesting that the latency decreases as well (Müller et al., 2019). To test this hypothesis, we analysed eIPSC peak latencies during 0.2 Hz stimulation for both genotypes and at both ages. Example current traces reveal a neurotransmission latency of 2.3 ms for P11 WT, 2.4 ms for P11 *Otof* KO, 1.4 ms for P38 WT, and 1.6 ms for P38 *Otof* KO (Fig. 12A). The scenario is graphically highlighted by artefact-aligned, peak-scaled eIPSCs (Fig. 12B). The similarity between genotypes was also displayed by the samples, i.e. the neurotransmission latency of *Otof* KOs was normal at P11 and P38 (Fig. 12C; P11 WTs: 2.4 ± 0.4 ms; P11 *Otof* KOs: 2.8 ± 0.5 ms, $n = 9, 11, P = 0.03$; P38 WTs: 1.6 ± 0.2 ms; P38 *Otof* KOs: 1.8 ± 0.3 ms, $n = 11, 11, P = 0.10$; unpaired *t* tests). During development, the latency shortened by $\sim 50\%$ in WTs and by $\sim 60\%$ in *Otof* KOs (Fig. 12C; $P = 3.3E-4, P = 1.5E-5$, unpaired *t* tests).

Taken together, the neurotransmission latency (assessed at low-frequency stimulation) shortens during development at MNTB–LSO inputs, as expected from higher release synchrony and faster receptor kinetics. At each age, the latency was normal in *Otof* KOs, suggesting that maturation depends neither on peripheral spontaneous activity nor on acoustic experience.

Impaired latency stability during sustained high-frequency stimulation in P38 *Otof* KOs

In a next step, we assessed latency stability during sustained high-frequency challenge. A stable latency is a temporal measure for high precision, robustness and fidelity (Brill et al., 2019; Krächan et al., 2017). Example current traces of a P11 WT and a P11 *Otof* KO neuron are amplitude colour-coded overlays of eIPSCs from the early and late phase of challenge trains (Fig. 13A). At 1–10 Hz, the latency remained stable throughout the train in both genotypes (Fig. 13B and C; check black circles below current traces in panels Aa and b). At 20–200 Hz, however, there was a trend of a latency increase during the challenge period, and the increase was frequency dependent (Fig. 13G; Table 4).

For P38, example current traces are shown in Fig. 13Da and b. Again, the latency remained quite stable up to 10 Hz challenge in each genotype (Fig. 13E and F; Table 4). At ≥ 20 Hz, however, it increased during challenge, and the increase was more pronounced in *Otof* KOs. It also increased with increasing stimulation frequency

Table 4. Total latency in WT and *Otof* KOs at P11 and P38

		Stimulation frequency (Hz)							
		1	2	5	10	20	50	100	200
Total latency	P11	98 ± 6	102 ± 9	101 ± 9	105 ± 10	110 ± 11	140 ± 16	n.d.	n.d.
	s₅₀₋₆₀ (%)								
	WT	(8)	(8)	(8)	(8)	(8)	(6)		
	P11	99 ± 8	100 ± 7	107 ± 10	105 ± 7	118 ± 11	131 ± 19	n.d.	n.d.
	<i>Otof</i> KO	(11)	(11)	(11)	(11)	(11)	(8)		
	P value	0.79	0.68	0.23	0.96	0.18	0.40	n.d.	n.d.
Total latency	P38	101 ± 3	103 ± 3	104 ± 3	106 ± 3	106 ± 5	112 ± 7	124 ± 9	141 ± 14
	s₅₀₋₆₀ (%)								
	WT	(13)	(13)	(13)	(13)	(12)	(11)	(11)	(11)
	P38	103 ± 6	106 ± 9	111 ± 13	111 ± 9	114 ± 7	136 ± 11	167 ± 20	154 ± 19
	<i>Otof</i> KO	(11)	(11)	(11)	(11)	(11)	(10)	(10)	(9)
	P value	0.45	0.39	0.11	0.08	0.02	3.9E-5	2.8E-6	0.13
	P value P11 WT vs. P38 WT	0.21	0.66	0.39	0.89	0.42	0.01	n.d.	n.d.
	P value P11 KO vs. P38 KO	0.23	0.09	0.44	0.12	0.41	0.52	n.d.	n.d.

Normalized latency values (means ± SD) were determined during s₅₀₋₆₀ of the challenge period. 100% represents the latency at the start of each train (cf. Fig. 12). Values in brackets depict number of cells. P values were determined by a t test. n.d., not determined due to a high number of synaptic failures. KO: knock-out; WT: wild type.

(Fig. 13G). Whereas the values increased to 114–167% until s₅₀₋₆₀ in *Otof* KOs at 20–100 Hz, they reached only 106–124% in WT (Table 4). Thus, the increase was 2.3- to 3-fold higher upon deafness (20 Hz: 14%/6%, 50 Hz: 36%/12%, 100 Hz: 67%/24%), implying weak stability and impairment in the release machinery, which result in the inability to cope with high-frequency challenge.

Reduced temporal precision of eIPSCs in P38 *Otof* KOs

A large quantal content forms the basis for temporally precise neurotransmission at MNTB-LSO inputs (Krächan et al., 2017). As a measure of precision, we determined the latency jitter during s₅₀₋₆₀ of stimulation (1–200 Hz). The jitter (= latency SD) increased similarly with the stimulus frequency in P11 WT and *Otof* KOs

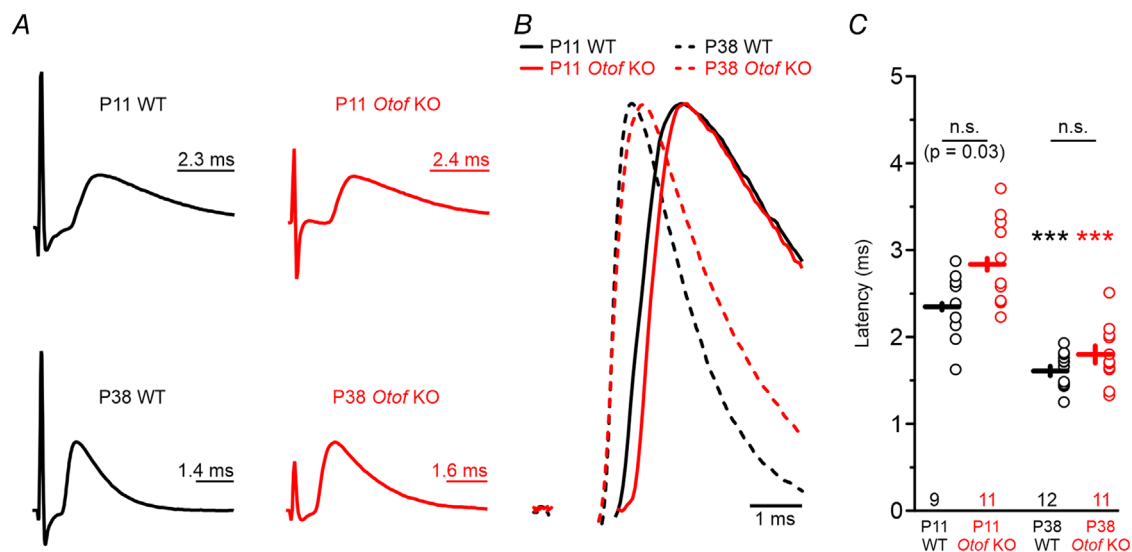


Figure 12. Normal developmental shortening of neurotransmission latency in *Otof* KOs
 A, example peak-scaled eIPSCs (graphical mean of 12 events) obtained at 0.2 Hz stimulation. Bars above eIPSCs indicate synaptic latency (from artefact peak to eIPSC peak). B, artefact-aligned and peak-scaled eIPSCs for direct latency comparison (stimulation artefacts blanked for clarity). C, statistics for latency. Numbers in plot are cell numbers. Statistical comparison between WT and *Otof* KOs was done via an unpaired t test. eIPSC: evoked inhibitory post-synaptic currents; KO: knock-out; WT: wild type.

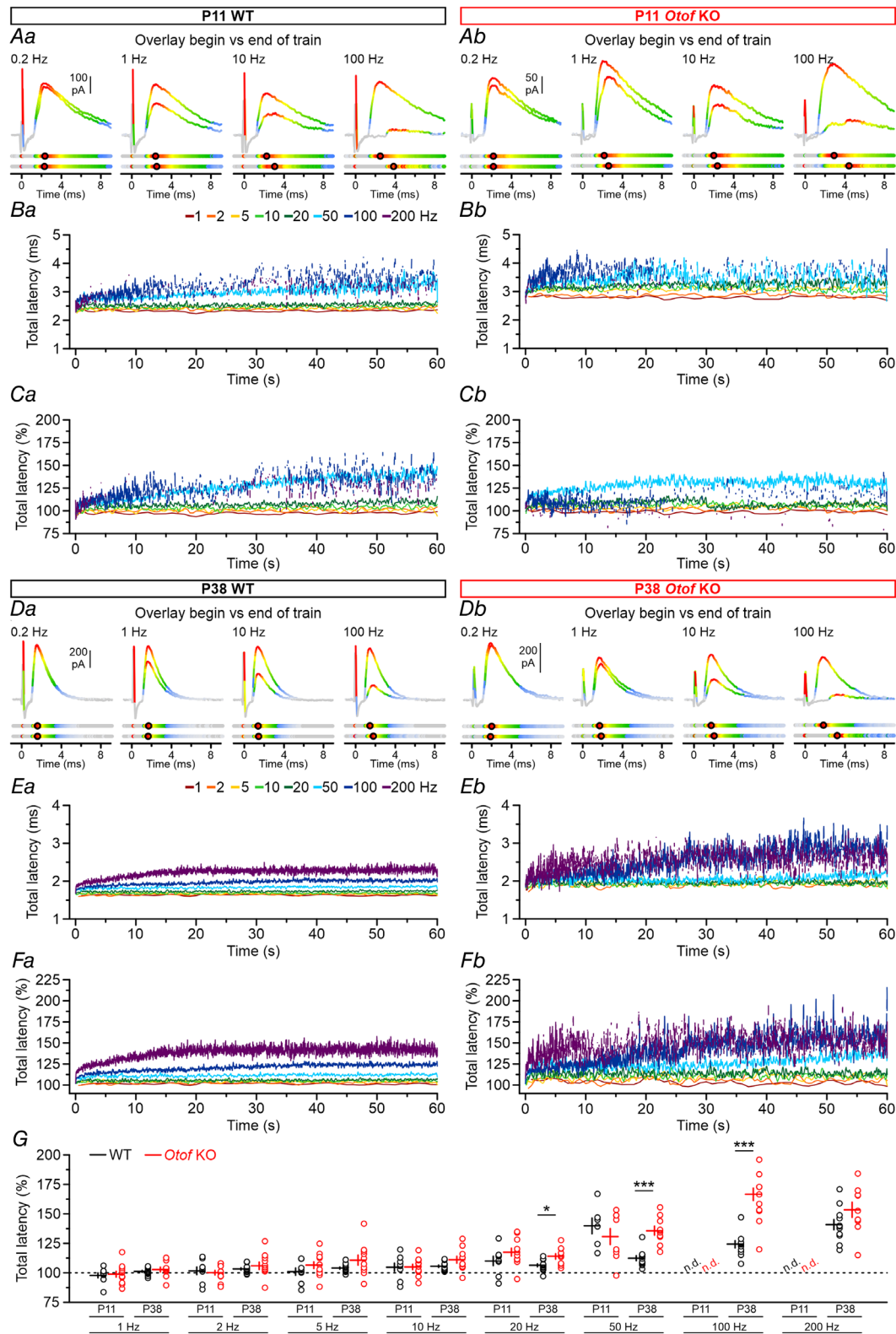


Figure 13. Increased latency shift during high-frequency challenge in P38 *Otof* KOs

A, overlay of example current traces from a P11 WT (Aa) and *Otof* KO (Ab) at the start and end of 0.2, 1, 10 and 100 Hz trains. Traces are colour-coded with a gradient from baseline to peak (grey to red). Colour-coded line plots below current traces belong to the traces above and depict artefacts at 0 ms and eIPSC peak amplitudes (black circles). B, time course of absolute total latency (NB: total latency = AP conduction time + synaptic latency) for P11

WTs (*Ba*) and P11 *Otof* KOs (*Bb*). *C*, as *B*, but for normalized latency. *D–F*, as *A–C*, but for P38. *G*, mean normalized latency during s_{50-60} of the challenge period. Statistical comparison between WT and *Otof* KO was done via an unpaired *t* test. n.d., not determined due to a high number of synaptic failures. Time courses are simple moving averages over three (1–2 Hz), five (5–20 Hz) or nine data points (50–200 Hz). Broken lines are due to many failures, prohibiting a statistical analysis. Details in Table 4. eIPSC: evoked inhibitory post-synaptic current; KO: knock-out; WT: wild type.

(Fig. 14*Aa* and *b*; black circles mark peak amplitudes). P38 inputs also showed a frequency-dependent increase in latency SD, but it was less pronounced in the WT at >10 Hz (Fig. 14*B*). Sample results confirmed the above observations and revealed statistically

distinguishable latency SD values at P11 for only one of five frequencies tested (Table 5). In contrast, P38 *Otof* KOs had a significantly higher latency SD than WT for seven of eight frequencies tested (Fig. 14*C*; Table 5).

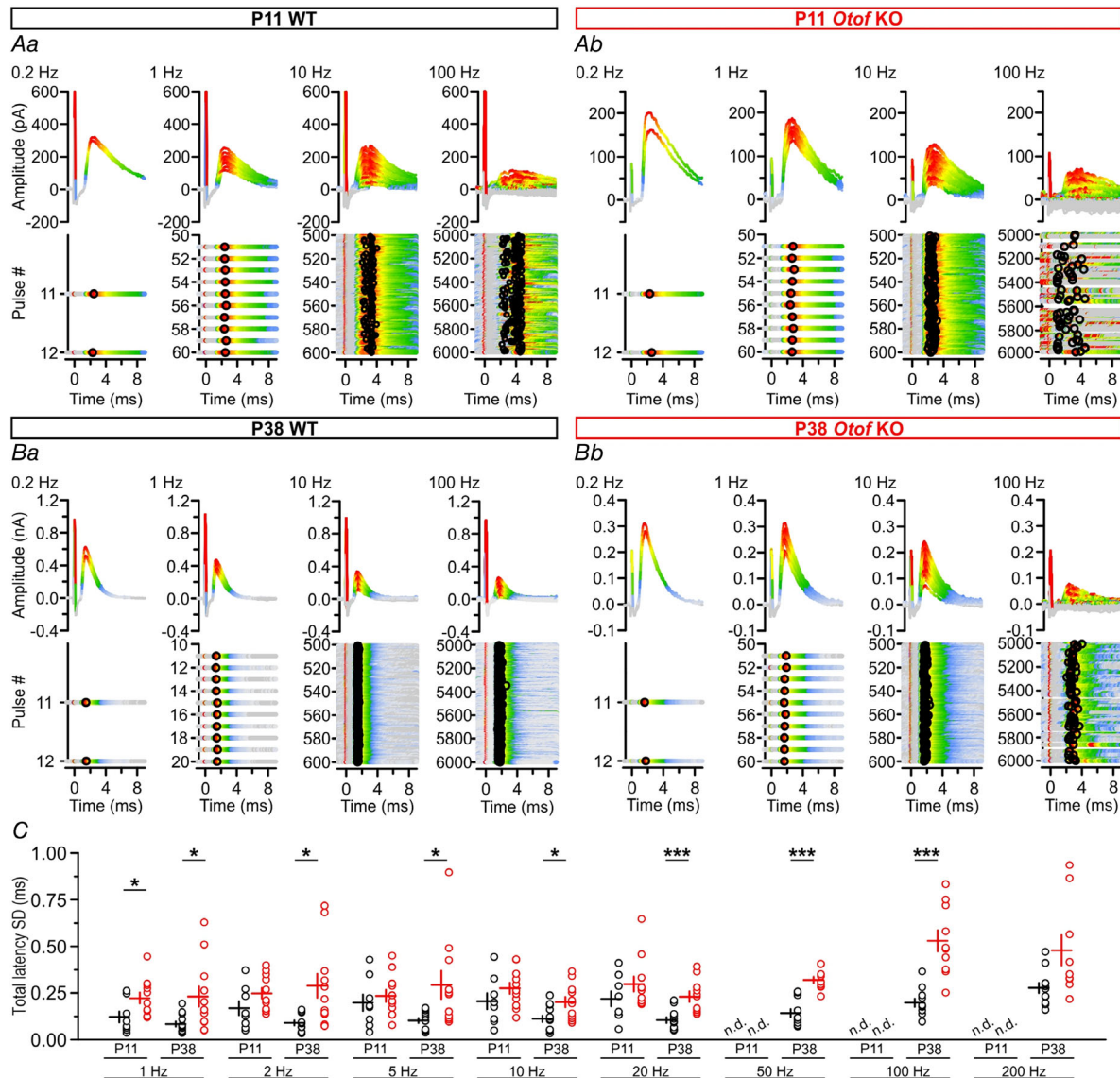


Figure 14. Lower precision of latency during sustained high-frequency challenge in P38 *Otof* KOs
A, example current traces from a WT (*Aa*) and an *Otof* KO neuron (*Ab*) at P11, depicting eIPSCs during s_{50-60} of 0.2, 1, 10 and 100 Hz trains. Traces are colour-coded with a gradient from baseline (grey) to peak (red). Black circles around red dots highlight the eIPSC peak. *B*, as *A*, but at P38. *C*, mean temporal precision during s_{50-60} of challenge. Statistical comparison was done via an unpaired *t* test. n.d., not determined, due to a large number of failures in most cells, which prohibited a continuous latency SD analysis. Details in Table 5. eIPSC: evoked inhibitory post-synaptic current; KO: knock-out; WT: wild type.

Table 5. Total latency SD in WT and *Otof* KO at P11 and P38

		Stimulation frequency (Hz)							
		1	2	5	10	20	50	100	200
Total latency SD	P11	0.12 ± 0.08	0.17 ± 0.11	0.20 ± 0.12	0.21 ± 0.12	0.22 ± 0.11	n.d.	n.d.	n.d.
	WT	(8)	(8)	(8)	(8)	(8)			
<i>s</i>₅₀₋₆₀ (ms)	P11	0.22 ± 0.1	0.25 ± 0.09	0.23 ± 0.11	0.28 ± 0.1	0.30 ± 0.13	n.d.	n.d.	n.d.
	<i>Otof</i> KO	(11)	(11)	(11)	(11)	(11)			
<i>P</i> value		0.04	0.12	0.52	0.21	0.22	n.d.	n.d.	n.d.
Total latency SD	P38	0.08 ± 0.05	0.09 ± 0.05	0.10 ± 0.05	0.11 ± 0.06	0.10 ± 0.05	0.14 ± 0.07	0.20 ± 0.07	0.28 ± 0.09
	WT	(13)	(13)	(13)	(13)	(12)	(11)	(11)	(11)
<i>s</i>₅₀₋₆₀ (ms)	P38	0.23 ± 0.18	0.29 ± 0.21	0.29 ± 0.23	0.20 ± 0.09	0.23 ± 0.09	0.32 ± 0.05	0.53 ± 0.18	0.48 ± 0.24
	<i>Otof</i> KO	(11)	(11)	(11)	(11)	(11)	(10)	(10)	(9)
<i>P</i> value		0.03	0.01	0.03	0.01	0.0005	6.0E-6	0.0002	0.05
<i>P</i> value P11 WT vs. P38 WT		0.22	0.10	0.09	0.09	0.04	n.d.	n.d.	n.d.
<i>P</i> value P11 KO vs. P38 KO		0.90	0.58	0.51	0.10	0.19	n.d.	n.d.	n.d.

Latency SD values to eIPSC peak (means ± SD) were determined during *s*₅₀₋₆₀ of the challenge period (*cf.* Fig. 13). Values in brackets depict number of cells. *P* values were determined by an unpaired two-tailed *t* test. n.d., not determined due to the high number of synaptic failures that permitted latency SD analysis. eIPSC: evoked inhibitory post-synaptic current; KO: knock-out; WT: wild type.

Taken together, a high RR enables P38 WT MNTB-LSO inputs to maintain a high quantal content during sustained high-frequency stimulation, thus achieving temporally precise synaptic transmission. Maturation of synaptic fidelity is largely absent in *Otof* KOs, as shown by a lower RR, more failures and temporal imprecision. Collectively, we conclude that acoustic experience is essential for proper development of resilient synaptic performance, which is likely a prerequisite for proper sound localization. In the following chapter, we will provide further evidence that the synaptic release and replenishment mechanisms appear to become impaired upon otoferlin loss, in contrast to AP robustness.

Normal maturation of AP latency in *Otof* KOs

The above analyses (Figs 12–14) assessed neurotransmission latency (= total latency) and thus did not differentiate between AP conduction time and synaptic latency. In order to disentangle one from the other, we addressed temporal aspects of AP conduction from the above antidromic experiments (*cf.* Fig. 4). The time course of AP latencies of P11 MNTB fibres during 60 s trains at frequencies of 1–200 Hz is illustrated in Fig. 15Aa and b (cells for which we obtained <100 APs during *s*₅₀₋₆₀ at ≥10 Hz were excluded from the analysis). WTs as well as *Otof* KOs displayed stable values throughout the 1 and 10 Hz trains, but increasing temporal instability towards higher values at 50, 100 and 200 Hz. For example, WT values at 10 Hz were 0.82 ms at the train's start and 0.88 ms during *s*₅₀₋₆₀ (Fig. 15Ca left; Table 6, increase of

7%, *n* = 13), whereas corresponding *Otof* KO values were 1.05 and 1.10 ms (Fig. 15Cb left, increase of 5%, *n* = 10). At 100 Hz, we observed 0.95 and 1.54 ms for WTs and 1.10 and 1.53 ms for *Otof* KOs (Fig. 15Ca and b right; Table 6, increases of 62% and 39%, *n* = 10 and 6). Thus, there appears to be no abnormality in AP conduction behaviour upon otoferlin loss around hearing onset.

At P38, AP latencies were not only considerably shorter than at P11, but also more stable during the trains (Fig. 15Ba and b). Values for 10 Hz were: WT 0.53 ms at the start, 0.55 ms during *s*₅₀₋₆₀; KO 0.54 ms at the start, 0.56 ms during *s*₅₀₋₆₀ (Fig. 15Da and b left panels; Table 6, 4% increase in each case, *n* = 13 and 16). Corresponding values for 100 Hz were: WT 0.53 ms at the start, 0.73 ms during *s*₅₀₋₆₀; KO 0.51 ms at the start, 0.82 ms during *s*₅₀₋₆₀ (Fig. 15Da and b, right panels; Table 6, 38% and 61% increase; *n* = 11 and 15). As at P11, no difference was obvious between genotypes, indicating that AP conduction properties develop normally despite deafness.

Our results on AP conduction properties allowed us to estimate the synaptic latency at MNTB-LSO inputs (synaptic latency = total latency – AP latency). We did this for 10 Hz and 100 Hz trains and compared between frequency, genotype and age (Fig. 15C–D). For each condition, the synaptic latency was ~2-fold longer than the AP latency (range 1.5–2.7 ms). During 10 Hz trains, the synaptic latency was quite stable, regardless of genotype and age (Fig. 15Ca and b, Da and b, left panels). In contrast, the 100 Hz challenge was accompanied by considerable instability. At this frequency, only the P38 WT MNTB-LSO inputs transmitted steadily and robustly,

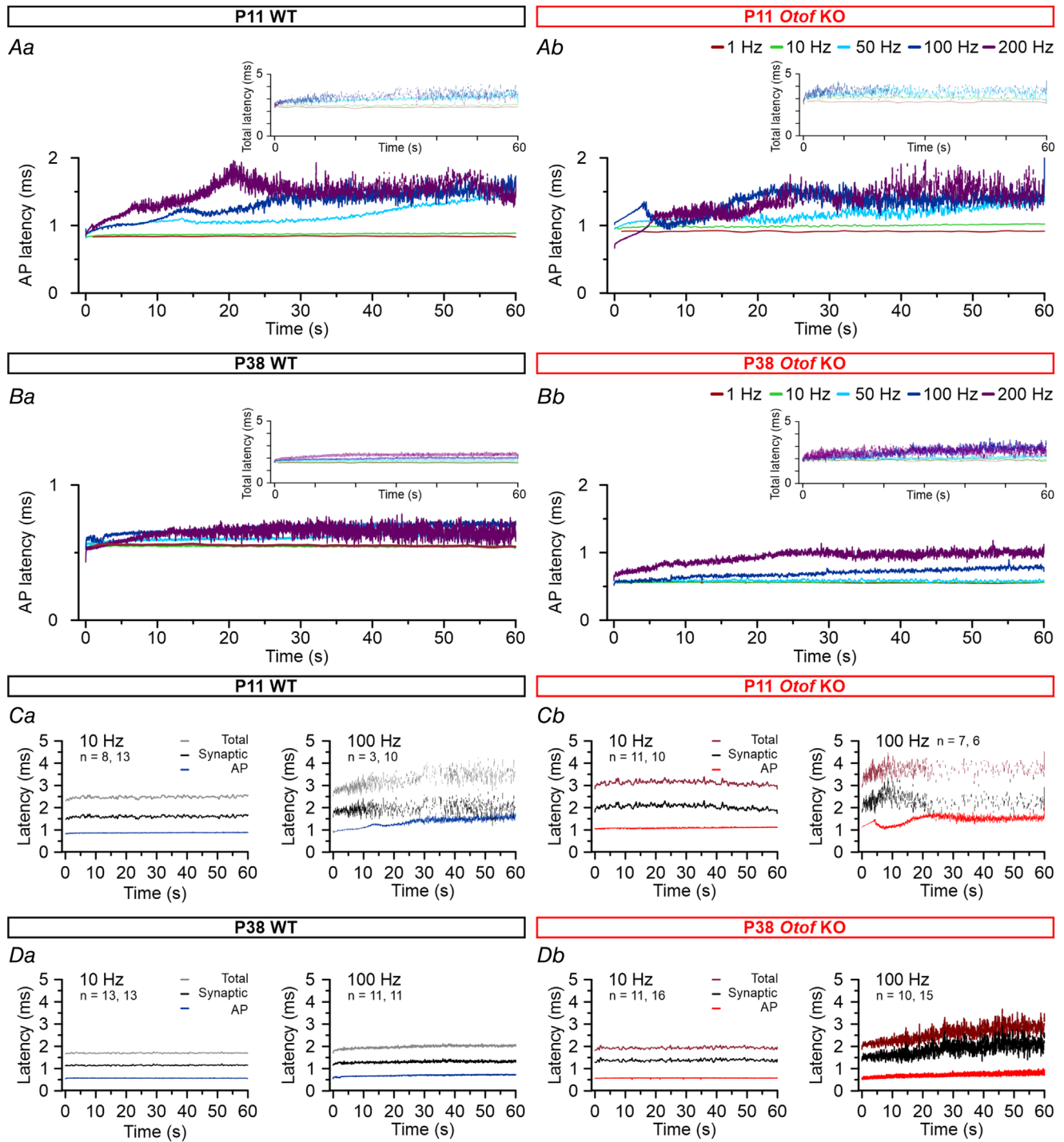


Figure 15. Normal maturation of AP latency in *Otof* KO
 A, time course of AP latency for P11 WT (Aa) and *Otof* KO (Ab). Insets show time course of total latency (cf. Fig. 12). B, as A, but at P38. Note different y-axis for P38 WT. C, time course of total latency, AP latency and estimated synaptic latency for P11 WT (Ca) and P11 *Otof* KO (Cb) for 10 Hz (left) and 100 Hz (right). D, as C, but at P38. (NB: total latency = AP latency + synaptic latency). Time courses are simple moving averages over three (1 Hz), five (10 Hz) or nine data points (50–200 Hz). Broken lines are due to many failures. *n* in C and D depict cell numbers for total latency, AP latency. AP: action potential; KO: knock-out; WT: wild type.

Table 6. AP conduction latency in WT and *Otof* KOs at P11 and P38

		Stimulation frequency (Hz)				
		1	10	50	100	200
AP conduction latency s₅₀₋₆₀ (ms)	P11	0.84 ± 0.01	0.88 ± 0.02	1.47 ± 0.13	1.54 ± 0.22	n.d.
	WT	(13)	(13)	(12)	(10)	
	P11	0.99 ± 0.03	1.10 ± 0.02	1.77 ± 0.14	1.53 ± 0.18	n.d.
	<i>Otof</i> KO	(11)	(11)	(7)	(6)	
	P value	0.24	0.12	0.44	0.56	n.d.
AP conduction latency s₅₀₋₆₀ (ms)	P38	0.55 ± 0.01	0.55 ± 0.01	0.67 ± 0.04	0.73 ± 0.04	0.65 ± 0.13
	WT	(13)	(13)	(13)	(11)	(8)
	P38	0.55 ± 0.01	0.56 ± 0.02	0.60 ± 0.04	0.82 ± 0.08	1.11 ± 0.12
	<i>Otof</i> KO	(16)	(16)	(15)	(15)	(12)
	P value	0.97	0.42	0.61	0.57	0.023
	P value P11 WT vs. P38 WT	0.05	3.5E-4	0.001	0.002	n.d.
	P value P11 KO vs. P38 KO	6.6E-4	0.007	0.02	0.015	n.d.

Latency values (means ± SD) were determined during s₅₀₋₆₀ of the challenge period. Values in brackets depict number of cells. P values were determined by unpaired *t* tests and were *post hoc* Šidák corrected. AP: action potential; KO: knock-out; WT: wild type.

with a synaptic latency of 1.16 ms at the train's start and 1.30 ms during s₅₀₋₆₀, whereas the other three cohorts displayed tremendous latency instability (Fig. 15Ca and b, Da and b, right panels). We conclude from these results that a stable AP latency appears to develop independently of acoustic experience, in contrast to the synaptic latency.

Discussion

Previously, we described impaired synaptic refinement in the MNTB–LSO circuit of *Otof* KOs at P11, around the onset of hearing (Müller et al., 2019). In the present study, we assessed the performance of this neurocircuit during sustained high-frequency stimulation in juvenile and young adult mice. Our main findings from WT and *Otof* KOs are: (1) at P11, MNTB–LSO inputs of *Otof* KOs perform normally; (2) between P11 and P38, increases of AP robustness, synaptic performance, RR of SVs and temporal precision of MNTB–LSO inputs occur in WT; (3) except for AP robustness, these parameters remain largely immature in *Otof* KOs; (4) more MNTB fibres converging on a given LSO neuron do not rescue the low performance of P38 *Otof* KOs; (5) computational modelling reveals RR deficits at single release sites in P38 *Otof* KOs; (6) a high RR and high AP robustness act together in enabling reliable and temporally precise neurotransmission in P38 WT, whereas P38 *Otof* KOs suffer particularly from a reduced RR. Collectively, we provide novel insights into the maturation of an inhibitory neurocircuit and its dependence on experience. We establish acoustic experience as the main contributor to

the developmental increase of its synaptic performance (Fig. 16).

P11 synapses perform normally in *Otof* KOs

Before hearing onset (~P12 in mice; Ehret, 1976, 1983), spontaneous spike activity propagates through the immature auditory system (Tritsch et al., 2007, 2010). Glycinergic MNTB–LSO synapses are strengthened between P4 and P11 (Bach & Kandler, 2020; Kim & Kandler, 2003). They become more resilient to synaptic depression during short trains (20 pulses), most likely due to an increased RRP (Alamilla & Gillespie, 2013). Spontaneous prehearing activity is drastically reduced in *Otof* KOs, leading to weaker MNTB–LSO inputs by P11 (Müller et al., 2019). Although the basic synaptic strength is lower, we found normal neurotransmission and an unaltered RR in *Otof* KOs at P11 (Figs 2, 9 and 10). These observations let us conclude that the neurotransmission performance develops independently from spontaneous prehearing activity. Consequently, its development appears to be uncoupled from the prehearing strengthening mechanisms. Furthermore, the similarity between WT and *Otof* KOs at P11 provides a valuable basis to study the impact of acoustic experience on this crucial parameter.

Acoustic experience is required to increase RR, but not the AP fidelity

Our P38 cohorts comprised the range of P31–49 and, therefore, WT have encountered ~3–5 weeks of

acoustic experience. By contrast, *Otof* KOs have not (Longo-Guess et al., 2007). We previously verified the absence of MNTB spiking upon acoustic stimulation (Müller et al., 2019). Thus, *Otof* KOs allow the differentiation of experience-dependent maturation from experience-independent maturation. In our previous study and the present one, we report normal acceleration of receptor kinetics, normal increase of SV release synchrony, normal latency shortening and normal maturation of AP fidelity in *Otof* KOs. In conclusion, these parameters are not shaped by acoustic experience, a result that we did not expect *a priori*. Collectively, there are differential effects of deafness on the functional maturation of auditory brainstem circuitry.

Acoustic experience impacts structural refinement, the maturation of biophysical properties, and the development of temporal integration within SOC circuits (Leake et al., 2006; Leao et al., 2004; Leao et al., 2005; Pilati et al., 2016; Walmsley et al., 2006; Werthat et al., 2008). A major novel finding of the present study is the considerable maturation of neurotransmission performance after hearing onset. This is particularly manifested by an ~ 8 -fold increase in the steady-state RR between P11 and P38 and an ~ 6 -fold increase when RR is normalized to a single site (Figs 9C, 10Da and 16). In contrast, RR increases only 2-fold in *Otof* KOs and this mild increase is not statistically significant (Figs 9C and 10Da). Nevertheless, we do not exclude a minor experience-independent or a compensatory mechanism

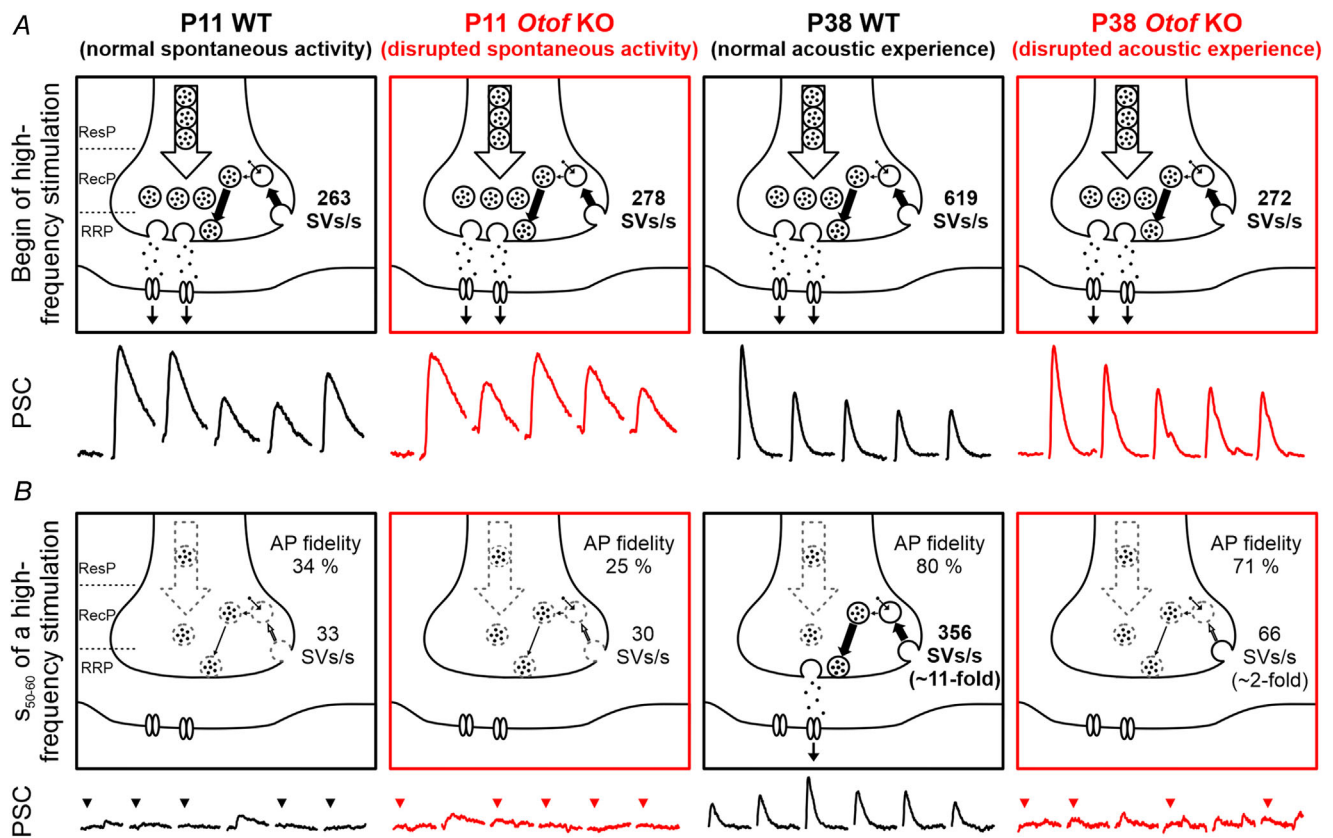


Figure 16. Proposed scenarios for neurotransmission during sustained high-frequency stimulation

A, SV replenishment at the start of 100 Hz challenge for WTs and *Otof* KOs at P11 and P38. SV replenishment is provided by the recycling pool (RecP), the reserve pool (ResP), and partly by the endocytic pathway. B, SV replenishment during s_{50-60} of 100 Hz challenge. RecP and ResP are likely depleted. Stippled lines indicate replenishment that is insufficient to maintain reliable neurotransmission. Between P11 and P38, replenishment capacity increases ~ 11 -fold in WTs (from 33 to 356 SVs/s), yet only ~ 2 -fold in *Otof* KOs (from 30 to 66 SVs/s). The extraordinarily high RR of 356 SVs/s in P38 WTs forms the basis for reliable neurotransmission during sustained high-frequency activity. eIPSCs are shown below schemes, triangles mark synaptic failures. RR values in panels are derived from the model (e.g. top left: 263 SVs/s). Notice that the replenishment capacity is most likely underestimated because of our strict identification criterion for release events. The issue is further addressed in the Discussion. eIPSC: evoked inhibitory post-synaptic current; KO: knock-out; RR: replenishment rate; SV: synaptic vesicle; WT: wild type.

in *Otof* KOs that leads to the slight RR increase. Even so, we conclude that the increase of RR mainly depends on acoustic experience.

No correlation between instantaneous AP failure rate and subsequent SV release

Our results of negligible recovery in the tens of milliseconds range (*cf.* Figs 5 and 11) are in good agreement with a classical study at calyx of Held synapses (7% after 50 ms, 53% after 1000 ms; Wu & Borst, 1999). They are also consistent with a recent SOC study which characterized inputs from the ventral CN to medial olivo-cochlear neurons (Romero & Trussell, 2021). The authors evoked a test postsynaptic current at various time intervals after a high-frequency pulse train (20 or 50 Hz) and found virtually no recovery from short-term depression at intervals <200 ms. Ultimately, they fitted the recovery behaviour by a mono-exponential function with a time constant of ~ 3 s. Our group has observed very similar recovery from short-term depression at MNTB–LSO inputs, namely only very minor fast recovery in the tens of milliseconds range (Weingarten, 2018).

In several auditory brainstem nuclei and at cerebellar climbing fibres, synapses show accelerated recovery when presynaptic Ca^{2+} that enters during the AP is elevated (Blitz et al., 2004; Foster et al., 2002; Wang & Kaczmarek, 1998; Yang & Xu-Friedman, 2008). In line with this, chelating presynaptic Ca^{2+} with extrinsic buffers decreases fast recovery. This has also been demonstrated in a ‘skipped-stimulus approach’ in which one stimulus in a high-frequency train was omitted (Yang & Xu-Friedman, 2015). Recovery of the eEPSC amplitude was affected for 60 ms in a Ca^{2+} -dependent manner. We reason that MNTB fibres are effectively protected from presynaptic Ca^{2+} build-up, particularly during the steady-state phase of ongoing high-frequency stimulation. Their complex repertoire of cytosolic Ca^{2+} buffers (Schwaller, 2010) is well described (Bazwinsky-Wutschke et al., 2016; Friauf, 1994; Lohmann & Friauf, 1996). Activity-related build-up of Ca_v channel inactivation or occluded clearance of release sites may also contribute to our results (Forsythe et al., 1998; Neher, 2010).

Considerable amplitude variation for eIPSCs to subsequent stimuli is not unique to the present study (*cf.* Figs 3*Bb*, 7*Ab* and 9*A*). Rather, substantial stimulus-to-stimulus variability has been reported by several groups at single MNTB–LSO fibres, even with low-frequency stimulation when the RRP likely remains large. eIPSC amplitudes can vary by several hundreds of picoampere and they depend heavily on the Cl^- driving force (Noh et al., 2010: 400 pA; Michalski et al., 2013: 1000 pA; Gjoni, Zenke et al., 2018: 150 pA; Müller et al.,

2019: 500 pA). It therefore appears that the variability reflects normal biological variance and not excitability problems.

Effective SV replenishment is the basis for high-fidelity synaptic transmission during sustained stimulation

High-fidelity transmission, a prominent feature of auditory brainstem synapses, is achieved by several structural and functional specializations (Oertel, 1999; Trussell, 1999; von Gersdorff & Borst, 2002; Yu & Goodrich, 2014). The specializations include a large N_{RRP} (~ 3000 SVs at the calyx of Held; Chen et al., 2015; Gan & Watanabe, 2018). However, high-frequency stimulation (>100 Hz) quickly depletes even this large RRP (Friauf et al., 2015), which then needs to be refilled (Rizzoli & Betz, 2005). Thus, a large RRP *per se* is insufficient for *sustained* synaptic transmission (over tens of seconds). A more likely factor imparting resilience to sustained neurotransmission is efficient SV replenishment (Fig. 9*E*; Delvendahl & Hallermann, 2016). For example, cerebellar mossy fibre-granule cell synapses have an ~ 10 -fold smaller RRP than the calyx of Held (Delvendahl & Hallermann, 2016), yet they achieve their exquisite fidelity through a high RR, even during sustained high-frequency stimulation (Delvendahl & Hallermann, 2016; Hallermann et al., 2010; Hallermann & Silver, 2013; Ritzau-Jost et al., 2014; Saviane & Silver, 2006).

SV replenishment is achieved mainly via two mechanisms: (1) SV recruitment from the recycling pool (RecP) and/or the reserve pool (ResP); (2) endocytosis to reform and refill SVs (Dutta Roy et al., 2014; Rizzoli & Betz, 2005; Südhof, 2004). During ongoing high-frequency stimulation for tens of seconds, as in the present study, both RecP and ResP become most likely depleted and SVs need to be reformed, including re-entry of refilled SVs into the RRP. We reason that replenishment during s_{50-60} of 100 Hz challenge is predominantly driven by endocytosis, for the following reasons. (1) SVs composing the RRP contribute to only $\sim 2\%$ of all SVs (Guo et al., 2015; Gan & Watanabe, 2018; Rizzoli & Betz, 2005; Sakaba & Neher, 2001; Sun & Wu, 2001). The combined RecP and ResP pool is ~ 50 -fold larger than the RRP. At MNTB–LSO synapses, RRP replenishment amounts to 50-fold after ~ 10 – 40 s of 100 Hz challenge, regardless of age or genotype (Fig. 10*Cb*). (2) Sustained stimulation upon blocked endocytosis results in gradually declining response amplitudes (Delgado et al., 2000). (3) SV replenishment via endocytosis is often regarded as the rate-limiting step during ongoing neurotransmission (Fernandez-Alfonso & Ryan, 2004; Südhof, 2004; but see Neher, 2010: release site clearance can be rate-limiting).

Table 7. SV release and replenishment at various synapse types

Synapse type	Steady-state current(pA)	q(pA)	Stimulation frequency(Hz)	Steady-state release(SVs/s)	Stimulation duration(s)	Number of sites	RR per site(SVs/s)
MNTB–LSO P11 WT	9 ^a	27 ^a	100 ^a	33 ^a	60 ^a	41 ^a	0.8 ^a
MNTB–LSO P11 <i>Otof</i> KO	7 ^a	23 ^a	100 ^a	30 ^a	60 ^a	43 ^a	0.7 ^a
MNTB–LSO P38 WT	79 ^a	22 ^a	100 ^a	359 ^a	60 ^a	80 ^a	4.5 ^a
MNTB–LSO P38 <i>Otof</i> KO	15 ^a	23 ^a	100 ^a	65 ^a	60 ^a	43 ^a	1.5 ^a
CN–LSOP11	-	19 ^b	50 ^b	100 ^b	60 ^b	156 ^b	0.6
LL–ICP11	-	20 ^b	50 ^b	1.5 ^b	60 ^b	18 ^b	0.1
CoH–MNTB~P17	6000 ^c	50 ^d	100 ^c	12,000	30 ^c	2700 ^e	4.4
cMFB–GC	6 ^f	15 ^f	100 ^f	40	60 ^f	5 ^f	8
CA3–CA1P11	-	23 ^g	50 ^g	3.5	60 ^g	160 ^g	0.02
EC–DGP11	-	20 ^g	50 ^g	5	60 ^g	55 ^g	0.1
NMJ	-	-	10	-	-	-	2 ^h

Steady-state release is the ratio $\frac{ePSC_{steady\ state}}{q}$, with $ePSC_{steady\ state} = steady\ state\ current \times stimulation\ frequency$. RR per site is the ratio $\frac{RR_{steady\ state}}{number\ of\ sites}$. The number of sites was derived from the number of SVs in the RRP (as assumed in computational modelling) or from variance–mean analysis at cMFB–GC synapses. Differences in the number of sites across synapse types can be explained by various numbers of activated input neurons. Notice that the numbers of SVs at MNTB–LSO inputs are most likely underestimated because of our strict identification criterion. This issue is further addressed in the *Discussion*.

^aThis study; ^bBrill et al., 2019, Fig. 12; ^cLucas et al., 2018, Fig. 7; ^dNeher, 2010; ^eChen et al., 2015, Table 3; ^fSaviane & Silver, 2006, Fig. 4C; ^gKrächan et al., 2017; ^hDelgado et al., 2000.

CN: cochlear nucleus; cMFB: cerebellar mossy fibre bouton; CoH: calyx of Held; DG: dentate gyrus; EC: entorhinal cortex; GC: granule cell; IC: inferior colliculus; KO: knock out; LL: lateral lemniscus; LSO: lateral superior olive; MNTB: medial nucleus of the trapezoid body; NMJ: neuromuscular junction of *Drosophila*; RR: replenishment rate; SV: synaptic vesicle.

Four mechanisms for retrieval of exocytosed SVs have been described: (1) kiss-and-run endocytosis; (2) clathrin-mediated endocytosis; (3) bulk endocytosis; (4) ultrafast endocytosis (Gan & Watanabe, 2018). They vary in terms of the *location* of membrane retrieval and – most prominently – in the *duration* of membrane retrieval (Kononenko & Haucke, 2015; Watanabe & Boucrot, 2017). Time scales amount to ~ 0.1 s for ultrafast endocytosis (Watanabe & Boucrot, 2017; Watanabe, Liu et al., 2013; Watanabe, Rost et al., 2013), ~ 1 s for kiss-and-run (Alabi & Tsien, 2013), ~ 10 – 30 s for clathrin-mediated exocytosis (Gan & Watanabe, 2018; Kononenko & Haucke, 2015) and ~ 10 – 60 s for bulk endocytosis (Gan & Watanabe, 2018). The mechanisms utilized at MNTB axon boutons are unknown. Our modelling reveals a reoccupation time of ~ 250 ms for single sites in P38 WTs (Fig. 10Eb), strongly arguing in favour of a rapid endocytosis mechanism, such as ultrafast endocytosis. However, membrane retrieval via ultrafast endocytosis lasts only ~ 100 ms, whereas subsequent generation of release-competent SVs needs ~ 5 s (Watanabe & Boucrot, 2017). The latter step is apparently not predominant for replenishment at WT P38 MNTB–LSO synapses, as it lasts ~ 20 -fold longer than the reoccupation time of ~ 250 ms (Fig. 10Eb). Rather, the short reoccupation time argues for specialized structural and/or functional adaptations to accelerate SV cycling processes at these synapses. It will be very interesting to identify these adaptations.

Taken together, the mechanisms for the extraordinarily robust performance of auditory (and other) synapses during *sustained* stimulation are enigmatic. It will be compelling to investigate MNTB–LSO synapses using the ‘flash-and-freeze’ technique (Watanabe, Liu et al., 2013; Watanabe, Rost et al., 2013). Interestingly, this technique has recently been adopted for sustained high-frequency stimulation in acute brain slices (Borges-Merjane et al., 2020).

Comparison of RR between MNTB–LSO synapses and other synapse types

Comparing RRs across various synapse types and neurocircuits is not straightforward, because regions and experimental conditions differ substantially (Hallermann & Silver, 2013). The numbers of stimulated fibres|boutons|release sites differ considerably, making a comparison of the absolute RR difficult, if not impossible. We used computational modelling to determine the RR at single sites, which can serve as a reliable normalization parameter for cross-comparisons. For P38 WT MNTB–LSO synapses, we obtained an RR of ~ 4.5 SVs/s per site (Fig. 10Da). In the following meta-analysis, we compare this value with other synapse types (Table 7).

Lucas et al. (2018) challenged calyx of Held–MNTB synapses at 100 Hz for 30 s; a steady-state RR of

~4.4 SVs/s can be deduced from their results (Table 7). For 100 Hz for 60 s stimulation of cerebellar mossy fibre bouton-granule cell synapses (Saviane & Silver, 2006), the same challenge conditions as in the present study, we estimate a steady-state RR of ~4.5 SVs/s per site (Table 7). In 10 Hz for 10 s stimulation experiments at the *Drosophila* neuromuscular junction (NMJ), Delgado et al. (2000) calculated an RR of ~2 SVs/s per site. At the zebrafish NMJ, 100 Hz for 20 s challenge causes mainly asynchronous SV release (Wen et al., 2016), indicating strong SV depletion and an RR too low to supply SVs for failure-free neurotransmission over tens of seconds. Recently, we employed 100 Hz for 60 s stimulation to compare the performance of MNTB–LSO inputs with two hippocampal and two auditory synapse types (CA3–CA1, entorhinal cortex–dentate gyrus (EC–DG), CN–LSO, lateral lemniscus–inferior colliculus (LL–IC); Brill et al., 2019; Krächan et al., 2017). The RR per site at CA3–CA1 and EC–DG synapses amounted to ~0.02 and ~0.1 SVs/s, respectively. These values are ~200-fold and ~50-fold lower than at MNTB–LSO synapses. CN–LSO and LL–IC synapses displayed an RR per site of 0.6 and 0.1 SVs/s (Table 7). These values are ~8-fold and ~50-fold lower than at MNTB–LSO synapses.

Taken together, the meta-analysis indicates an extraordinarily high RR per site at MNTB–LSO synapses, imparting more robustness and reliability to synaptic transmission than at NMJ, LL–IC, CN–LSO, EC–DG and CA3–CA1 synapses. Furthermore, the high RR at the inhibitory MNTB–LSO synapses appears to be on a par with that at excitatory calyx of Held and excitatory cerebellar mossy fibre terminals (both being ultra-high performers).

Technical considerations: detection failures

Our analysis of empirical eIPSC amplitudes as a function of preceding failures (Fig. 5) showed virtually no relationship up to 120 ms. Computing amplitudes via a probabilistic model explained the experimental findings (Fig. 11 and Suppl. document ‘Interactive modelling of quantal content.xlsm’). AP failures as well as synaptic failures contribute to transmission failures, and detection failures form a third source. Indeed, because of our strict threshold (>1.5-fold q , see *Methods*), we most likely overestimated the failures. Moreover, during sustained high-frequency stimulation, minimally filled SVs may be exocytosed due to insufficient presynaptic control of q , resulting in metaphorical firing of blank cartridges. Even if the molecular processes of SV replenishment (filling of empty sites) and SV exocytosis are effective, the strength of synaptic transmission will be drastically reduced. For example, if q decreases to 11 pA (half of the normal q of 22 pA), a simultaneous exocytosis of at least

three SVs would be required to surpass the threshold criterion. Our analysis therefore fails to detect such small ‘subthreshold’ responses. Nevertheless, we want to point out that the problem of detection failures affects only the results demonstrated in Figs 3, 5 and 7. The results demonstrated in Figs 9 and 10, however, are not affected, i.e. our comparison of replenishment rates across cohorts needs no correction.

Implications for human deafness

Among the >120 genes involved in hearing impairment (<http://hereditaryhearingloss.org>), mutations of the human *OTOF* gene occur at a frequency of ~2–7%, i.e. much higher than average (Duman et al., 2011; Iwasa et al., 2013; Iwasa et al., 2019; Rodriguez-Ballesteros et al., 2008). Might the results of our study have any implications for the relatively large cohort of deaf patients carrying *OTOF* mutations? Deaf patients carrying bilateral cochlear implants (CIs) have only very limited spatial hearing ability, and their horizontal-plane sound localization strongly relies on ILD cues (Aronoff et al., 2010; Mayo & Goupell, 2020). They can coarsely localize a single source in quiet, but their performance declines rapidly in the presence of other sound (Williges et al., 2018). Due to the limited dynamic range of hearing aids, ILD information is reduced (Kerber & Seeber, 2012) and it becomes difficult to create an auditory scene or to segregate target speech from spatially separated noise.

As shown in this study, MNTB–LSO inputs, which participate in ILD analysis, display impaired performance in *Otof* KO mice, particularly during ongoing stimulation. It is compelling to investigate whether the lower performance, a result of lacking acoustic experience, is irreversible. Supplying *Otof* KOs with CIs or restoring hearing via gene therapy are possible approaches (Akil & Lustig, 2019; Al-Moyed et al., 2019; Tertrais et al., 2019). Both approaches may need to consider the various (critical) periods during which synaptic function develops, both through activity-dependent and activity-independent mechanisms. Considering the characteristic specificities of these periods will likely help to optimize CI strategies and to minimize the impairments of deaf patients.

Conclusions

The present study and our previous one (Müller et al., 2019) shine light on activity-dependent and activity-independent maturation of an inhibitory brain-stem circuit involved in sound localization (Friauf & Lohmann, 1999; Kandler et al., 2009). During the prehearing period, elimination and strengthening of MNTB–LSO synapses depend on spontaneous activity.

After hearing onset, sound-evoked activity shapes the robustness and temporal precision of neurotransmission. Nevertheless, several parameters develop normally in *Otof* KOs, implying genetic determination and, therefore, some independence of acoustic experience. Overall, an interplay of activity-dependent and activity-independent processes orchestrates the maturation of this inhibitory brainstem circuit. We are still at the beginning of better comprehending the complexity of these processes.

References

- Abdi, H. (2007). The Bonferroni and Šidák corrections for multiple comparisons. In E. Salkind (ed.), *Encyclopedia of measurement and statistics* (pp. 103–107). Sage, Thousand Oaks.
- Akil, O., & Lustig, L. (2019). AAV-mediated gene delivery to the inner ear. *Methods in Molecular Biology*, **1950**, 271–282.
- Al-Moyed, H., Cepeda, A. P., Jung, S., Moser, T., Kugler, S., & Reisinger, E. (2019). A dual-AAV approach restores fast exocytosis and partially rescues auditory function in deaf *otof* knock-out mice. *EMBO Molecular Medicine*, **11**, e9396.
- Alabi, A. A., & Tsien, R. W. (2013). Perspectives on kiss-and-run: Role in exocytosis, endocytosis, and neurotransmission. *Annual Review of Physiology*, **75**, 393–422.
- Alamilla, J., & Gillespie, D. C. (2013). Maturation of calcium-dependent GABA, glycine, and glutamate release in the glycinergic MNTB-LSO pathway. *Plos One*, **8**, e75688.
- Aronoff, J. M., Yoon, Y. S., Freed, D. J., Vermiglio, A. J., Pal, L., & Soli, S. D. (2010). The use of interaural time and level difference cues by bilateral cochlear implant users. *The Journal of the Acoustical Society of America*, **127**, EL87–EL92.
- Ashida, G., Tollin, D. J., & Kretzberg, J. (2017). Physiological models of the lateral superior olive. *Plos Computational Biology*, **13**, e1005903.
- Bach, E. C., & Kandler, K. (2020). Long-term potentiation of glycinergic synapses by semi-natural stimulation patterns during tonotopic map refinement. *Science Reports*, **10**, 16899.
- Bazwinsky-Wutschke, I., Härtig, W., Kretzschmar, R., & Rübsamen, R. (2016). Differential morphology of the superior olivary complex of *Meriones unguiculatus* and *Mono-delphis domestica* revealed by calcium-binding proteins. *Brain Structure & Function*, **221**, 4505–4523.
- Beiderbeck, B., Myoga, M. H., Müller, N. I. C., Callan, A. R., Friauf, E., Grothe, B., & Pecka, M. (2018). Precisely timed inhibition facilitates action potential firing for spatial coding in the auditory brainstem. *Nature Communication*, **9**, 1771.
- Beurg, M., Fettiplace, R., Nam, J. H., & Ricci, A. J. (2009). Localization of inner hair cell mechanotransducer channels using high-speed calcium imaging. *Nature Neuroscience*, **12**, 553–558.
- Blitz, D. M., Foster, K. A., & Regehr, W. G. (2004). Short-term synaptic plasticity: A comparison of two synapses. *Nature Reviews Neuroscience*, **5**, 630–640.
- Borges-Merjane, C., Kim, O., & Jonas, P. (2020). Functional electron microscopy, “Flash and Freeze,” of identified cortical synapses in acute brain slices. *Neuron*, **105**, 992–1006.e6.
- Boudreau, J. C., & Tsuchitani, C. (1968). Binaural interaction in the cat superior olive S segment. *Journal of Neurophysiology*, **31**, 442–454.
- Brill, S. E., Janz, K., Singh, A., & Friauf, E. (2019). Considerable differences between auditory medulla, auditory midbrain, and hippocampal synapses during sustained high-frequency stimulation: Exceptional vesicle replenishment restricted to sound localization circuit. *Hearing Research*, **381**, 107771.
- Caird, D., & Klinke, R. (1983). Cat superior olivary complex (SOC): The basis of binaural information processing. In R. Klinke & R. Hartmann (eds.), *Hearing: Physiological bases and psychophysics* (pp. 216–223). Springer.
- Cao, X. J., McGinley, M. J., & Oertel, D. (2008). Connections and synaptic function in the posteroventral cochlear nucleus of deaf jerker mice. *Journal of Comparative Neurology*, **510**, 297–308.
- Chen, Z., Das, B., Nakamura, Y., DiGregorio, D. A., & Young, S. M. J. (2015). Ca²⁺ channel to synaptic vesicle distance accounts for the readily releasable pool kinetics at a functionally mature auditory synapse. *Journal of Neuroscience*, **35**, 2083–2100.
- Clause, A., Kim, G., Sonntag, M., Weisz, C. J., Vetter, D. E., Rübsamen, R., & Kandler, K. (2014). The precise temporal pattern of prehearing spontaneous activity is necessary for tonotopic map refinement. *Neuron*, **82**, 822–835.
- Delgado, R., Maureira, C., Oliva, C., Kidokoro, Y., & Labarca, P. (2000). Size of vesicle pools, rates of mobilization, and recycling at neuromuscular synapses of a *Drosophila* mutant, *shibire*. *Neuron*, **28**, 941–953.
- Delvendahl, I., & Hallermann, S. (2016). The cerebellar mossy fiber synapse as a model for high-frequency transmission in the mammalian CNS. *Trends in Neuroscience (Tins)*, **39**, 722–737.
- Duman, D., Sirmaci, A., Cengiz, F. B., Ozdag, H., & Tekin, M. (2011). Screening of 38 genes identifies mutations in 62% of families with nonsyndromic deafness in Turkey. *Genetic Testing and Molecular Biomarkers*, **15**, 29–33.
- Dutta Roy, R., Stefan, M. I., & Rosenmund, C. (2014). Biophysical properties of presynaptic short-term plasticity in hippocampal neurons: Insights from electrophysiology, imaging and mechanistic models. *Frontiers in Cellular Neuroscience*, **8**, 141.
- Ehret, G. (1976). Development of absolute auditory thresholds in the house mouse (*Mus musculus*). *Journal of the American Academy of Audiology*, **1**, 179–184.
- Ehret, G. (1983). Development of hearing and response behavior to sound stimuli. In R. Romand (ed.), *Development of auditory and vestibular systems* (pp. 211–237). Academic Press, New York.
- Elmqvist, D., & Quastel, D. M. J. (1965). A quantitative study of end-plate potentials in isolated human muscle. *Journal of Physiology*, **178**, 505–529.
- Fernandez-Alfonso, T., & Ryan, T. A. (2004). The kinetics of synaptic vesicle pool depletion at CNS synaptic terminals. *Neuron*, **41**, 943–953.

- Fischer, A. U., Müller, N. I. C., Deller, T., Del Turco, D., Fisch, J. O., Griesemer, D., Kattler, K., Maraslioglu, A., Roemer, V., Xu-Friedman, M. A., Walter, J., & Friauf, E. (2019). GABA is a modulator, rather than a classical transmitter, in the medial nucleus of the trapezoid body-lateral superior olive sound localization circuit. *Journal of Physiology*, **597**, 2269–2295.
- Ford, M. C., Alexandrova, O., Cossell, L., Stange-Marten, A., Sinclair, J., Kopp-Scheinflug, C., Pecka, M., Attwell, D., & Grothe, B. (2015). Tuning of Ranvier node and internode properties in myelinated axons to adjust action potential timing. *Nature Communication*, **6**, 8073.
- Forsythe, I. D., Tsujimoto, T., Barnes-Davies, M., Cuttle, M. F., & Takahashi, T. (1998). Inactivation of presynaptic calcium current contributes to synaptic depression at a fast central synapse. *Neuron*, **20**, 797–807.
- Foster, K. A., Kreitzer, A. C., & Regehr, W. G. (2002). Interaction of postsynaptic receptor saturation with presynaptic mechanisms produces a reliable synapse. *Neuron*, **36**, 1115–1126.
- Franken, T. P., Joris, P. X., & Smith, P. H. (2018). Principal cells of the brainstem's interaural sound level detector are temporal differentiators rather than integrators. *Elife*, **7**, e33854.
- Friauf, E. (1994). Distribution of calcium-binding protein calbindin-D28k in the auditory system of adult and developing rats. *Journal of Comparative Neurology*, **349**, 193–211.
- Friauf, E., Fischer, A. U., & Fuhr, M. F. (2015). Synaptic plasticity in the auditory system: A review. *Cell and Tissue Research*, **361**, 177–213.
- Friauf, E., Krächan, E. G., & Müller, N. I. C. (2019). Lateral superior olive: Organization, development, and plasticity. In K. Kandler (ed.), *Auditory brainstem*, Oxford University Press, New York.
- Friauf, E., & Lohmann, C. (1999). Development of auditory brainstem circuitry. Activity-dependent and activity-independent processes. *Cell and Tissue Research*, **297**, 187–195.
- Gan, Q., & Watanabe, S. (2018). Synaptic vesicle endocytosis in different model systems. *Frontiers in Cellular Neuroscience*, **12**, 171.
- Gjoni, E., Aguet, C., Sahlender, D. A., Knott, G., & Schneggenburger, R. (2018). Ultrastructural basis of strong unitary inhibition in a binaural neuron. *Journal of Physiology*, **596**, 4969–4982.
- Gjoni, E., Zenke, F., Bouhours, B., & Schneggenburger, R. (2018). Specific synaptic input strengths determine the computational properties of excitation-inhibition integration in a sound localization circuit. *Journal of Physiology*, **596**, 4945–4967.
- Glendenning, K. K., Hutson, K. A., Nudo, R. J., & Masterton, R. B. (1985). Acoustic chiasm II: Anatomical basis of binaurality in lateral superior olive of cat. *Journal of Comparative Neurology*, **232**, 261–285.
- Grothe, B., & Pecka, M. (2014). The natural history of sound localization in mammals - a story of neuronal inhibition. *Frontiers in Neural Circuits*, **8**, 116.
- Grundy, D. (2015). Principles and standards for reporting animal experiments in The Journal of Physiology and Experimental Physiology. *Journal of Physiology*, **593**, 2547–2549.
- Guo, J., Ge, J. L., Hao, M., Sun, Z. C., Wu, X. S., Zhu, J. B., Wang, W., Yao, P. T., Lin, W., & Xue, L. (2015). A three-pool model dissecting readily releasable pool replenishment at the calyx of Held. *Science Reports*, **5**, 9517.
- Hallermann, S., Fejtova, A., Schmidt, H., Weyhermüller, A., Silver, R. A., Gundelfinger, E. D., & Eilers, J. (2010). Bassoon speeds vesicle reloading at a central excitatory synapse. *Neuron*, **68**, 710–723.
- Hallermann, S., & Silver, R. A. (2013). Sustaining rapid vesicular release at active zones: Potential roles for vesicle tethering. *Trends in Neuroscience (Tins)*, **36**, 185–194.
- Heidrych, P., Zimmermann, U., Kuhn, S., Franz, C., Engel, J., Duncker, S. V., Hirt, B., Pusch, C. M., Ruth, P., Pfister, M., Marcotti, W., Blin, N., & Knipper, M. (2009). Otoferlin interacts with myosin VI: Implications for maintenance of the basolateral synaptic structure of the inner hair cell. *Human Molecular Genetics*, **18**, 2779–2790.
- Helfert, R. H., & Schwartz, I. R. (1986). Morphological evidence for the existence of multiple neuronal classes in the cat lateral superior olivary nucleus. *Journal of Comparative Neurology*, **244**, 533–549.
- Hintze, A., Gültas, M., Semmelhack, E. A., & Wichmann, C. (2021). Ultrastructural maturation of the endbulb of Held active zones comparing wild-type and otoferlin-deficient mice. *iScience*, **24**, 102282.
- Hirtz, J. J., Braun, N., Griesemer, D., Hannes, C., Janz, K., Löhrke, S., Müller, B., & Friauf, E. (2012). Synaptic refinement of an inhibitory topographic map in the auditory brainstem requires functional Ca_v1.3 calcium channels. *Journal of Neuroscience*, **32**, 14602–14616.
- Iwasa, Y., Nishio, S. Y., Yoshimura, H., Kanda, Y., Kumakawa, K., Abe, S., Naito, Y., Nagai, K., & Usami, S. (2013). OTOF mutation screening in Japanese severe to profound recessive hearing loss patients. *Bmc Medical Genetics*, **14**, 95.
- Iwasa, Y. I., Nishio, S. Y., Sugaya, A., Kataoka, Y., Kanda, Y., Taniguchi, M., Nagai, K., Naito, Y., Ikezono, T., Horie, R., Sakurai, Y., Matsuoka, R., Takeda, H., Abe, S., Kihara, C., Ishino, T., Morita, S. Y., Iwasaki, S., Takahashi, M., ... Usami, S. I. (2019). OTOF mutation analysis with massively parallel DNA sequencing in 2,265 Japanese sensorineural hearing loss patients. *Plos One*, **14**, e0215932.
- Joris, P. X., & van derHeijden, M. (2019). Early binaural hearing: The comparison of temporal differences at the two ears. *Annual Review of Neuroscience*, **42**, 433–457.
- Kandler, K., Clause, A., & Noh, J. (2009). Tonotopic reorganization of developing auditory brainstem circuits. *Nature Neuroscience*, **12**, 711–717.
- Kandler, K., & Friauf, E. (1995). Development of glycinergic and glutamatergic synaptic transmission in the auditory brainstem of perinatal rats. *Journal of Neuroscience*, **15**, 6890–6904.
- Kemmer, G., & Keller, S. (2010). Nonlinear least-squares data fitting in Excel spreadsheets. *Nature Protocols*, **5**, 267–281.

- Kerber, S., & Seeber, B. U. (2012). Sound localization in noise by normal-hearing listeners and cochlear implant users. *Ear and Hearing*, **33**, 445–457.
- Kim, G., & Kandler, K. (2003). Elimination and strengthening of glycinergic/GABAergic connections during tonotopic map formation. *Nature Neuroscience*, **6**, 282–290.
- Kim, G., & Kandler, K. (2010). Synaptic changes underlying the strengthening of GABA/glycinergic connections in the developing lateral superior olive. *Neuroscience*, **171**, 924–933.
- Kononenko, N. L., & Haucke, V. (2015). Molecular mechanisms of presynaptic membrane retrieval and synaptic vesicle reformation. *Neuron*, **85**, 484–496.
- Körber, C., Horstmann, H., Venkataramani, V., Herrmannsdörfer, F., Kremer, T., Kaiser, M., Schwenger, D. B., Ahmed, S., Dean, C., Dresbach, T., & Kuner, T. (2015). Modulation of presynaptic release probability by the vertebrate-specific protein mover. *Neuron*, **87**, 521–533.
- Krächan, E. G., Fischer, A. U., Franke, J., & Friauf, E. (2017). Synaptic reliability and temporal precision are achieved via high quantal content and effective replenishment: Auditory brainstem versus hippocampus. *Journal of Physiology*, **595**, 839–864.
- Kramer, F., Griesemer, D., Bakker, D., Brill, S., Franke, J., Frotscher, E., & Friauf, E. (2014). Inhibitory glycinergic neurotransmission in the mammalian auditory brainstem upon prolonged stimulation: Short-term plasticity and synaptic reliability. *Frontiers in Neural Circuits*, **8**, 14.
- Lalor, E. C., Power, A. J., Reilly, R. B., & Foxe, J. J. (2009). Resolving precise temporal processing properties of the auditory system using continuous stimuli. *Journal of Neurophysiology*, **102**, 349–359.
- Leake, P. A., Hradek, G. T., Chair, L., & Snyder, R. L. (2006). Neonatal deafness results in degraded topographic specificity of auditory nerve projections to the cochlear nucleus in cats. *Journal of Comparative Neurology*, **497**, 13–31.
- Leao, R. N., Berntson, A., Forsythe, I. D., & Walmsley, B. (2004). Reduced low-voltage activated K⁺ conductances and enhanced central excitability in a congenitally deaf (*dn/dn*) mouse. *Journal of Physiology*, **559**, 25–33.
- Leao, R. N., Svahn, K., Berntson, A., & Walmsley, B. (2005). Hyperpolarization-activated (I_h) currents in auditory brainstem neurons of normal and congenitally deaf mice. *European Journal of Neuroscience*, **22**, 147–157.
- Lee, H., Bach, E., Noh, J., Delpire, E., & Kandler, K. (2016). Hyperpolarization-independent maturation and refinement of GABA/glycinergic connections in the auditory brain stem. *Journal of Neurophysiology*, **115**, 1170–1182.
- Lohmann, C., & Friauf, E. (1996). Distribution of the calcium-binding proteins parvalbumin and calretinin in the auditory brainstem of adult and developing rats. *Journal of Comparative Neurology*, **367**, 90–109.
- Longo-Guess, C., Gagnon, L. H., Bergstrom, D. E., & Johnson, K. R. (2007). A missense mutation in the conserved C2B domain of otoferlin causes deafness in a new mouse model of DFNB9. *Hearing Research*, **234**, 21–28.
- Lucas, S. J., Michel, C. B., Marra, V., Smalley, J. L., Hennig, M. H., Graham, B. P., & Forsythe, I. D. (2018). Glucose and lactate as metabolic constraints on presynaptic transmission at an excitatory synapse. *Journal of Physiology*, **596**, 1699–1721.
- Magnusson, A. K., Kapfer, C., Grothe, B., & Koch, U. (2005). Maturation of glycinergic inhibition in the gerbil medial superior olive after hearing onset. *Journal of Physiology*, **568**, 497–512.
- Mahdih, N., Shirkavand, A., Rabbani, B., Tekin, M., Akbari, B., Akbari, M. T., & Zeinali, S. (2012). Screening of *OTOF* mutations in Iran: A novel mutation and review. *International Journal of Pediatric Otorhinolaryngology*, **76**, 1610–1615.
- Masterton, B., Jane, J. A., & Diamond, I. T. (1967). Role of brainstem auditory structures in sound localization. I. Trapezoid body, superior olive, and lateral lemniscus. *Journal of Neurophysiology*, **30**, 341–359.
- Mayo, P. G., & Goupell, M. J. (2020). Acoustic factors affecting interaural level differences for cochlear-implant users. *The Journal of the Acoustical Society of America*, **147**, EL357–EL362.
- Mendoza Schulz, A., Jing, Z., Sanchez Caro, J. M., Wetzel, F., Dresbach, T., Strenzke, N., Wichmann, C., & Moser, T. (2014). Bassoon-disruption slows vesicle replenishment and induces homeostatic plasticity at a CNS synapse. *EMBO Journal*, **33**, 512–527.
- Michalski, N., Babai, N., Renier, N., Perkel, D. J., Chedotal, A., & Schneggenburger, R. (2013). Robo3-driven axon mid-line crossing conditions functional maturation of a large commissural synapse. *Neuron*, **78**, 855–868.
- Michalski, N., Goutman, J. D., Auclair, S. M., Boutet de Monvel, J., Tertrais, M., Emptoz, A., Parrin, A., Nouaille, S., Guillon, M., Sachse, M., Ciric, D., Bahloul, A., Hardelin, J. P., Sutton, R. B., Avan, P., Krishnakumar, S. S., Rothman, J. E., Dulon, D., Safieddine, S., & Petit, C. (2017). Otoferlin acts as a Ca²⁺ sensor for vesicle fusion and vesicle pool replenishment at auditory hair cell ribbon synapses. *Elife*, **6**, e31013.
- Miki, T., Nakamura, Y., Malagon, G., Neher, E., & Marty, A. (2018). Two-component latency distributions indicate two-step vesicular release at simple glutamatergic synapses. *Nature Communication*, **9**, 3943.
- Moser, T., & Starr, A. (2016). Auditory neuropathy—neural and synaptic mechanisms. *Nature reviews Neurology*, **12**, 135–149.
- Müller, N. I. C., Sonntag, M., Maraslioglu, A., Hirtz, J. J., & Friauf, E. (2019). Topographic map refinement and synaptic strengthening of a sound localization circuit require spontaneous peripheral activity. *Journal of Physiology*, **597**, 5469–5493.
- Mukherjee, D., Meng, X., Kao, J. P. Y., & Kanold, P. O. (2021). Impaired hearing and altered subplate circuits during the first and second postnatal weeks of otoferlin-deficient mice. *Cerebral Cortex*, <https://doi.org/10.1093/cercor/bhab383>.
- Neher, E. (2010). What is rate-limiting during sustained synaptic activity: Vesicle supply or the availability of release sites. *Frontiers in Synaptic Neuroscience*, **2**, 144.

- Neher, E. (2017). Some subtle lessons from the calyx of Held synapse. *Biophysical Journal*, **112**, 215–223.
- Noh, J., Seal, R. P., Garver, J. A., Edwards, R. H., & Kandler, K. (2010). Glutamate co-release at GABA/glycinergic synapses is crucial for the refinement of an inhibitory map. *Nature Neuroscience*, **13**, 232–238.
- Oertel, D. (1999). The role of timing in the brain stem auditory nuclei of vertebrates. *Annual Review of Physiology*, **61**, 497–519.
- Owrutsky, Z. L., Benichoux, V., & Tollin, D. J. (2021). Binaural hearing by the mammalian auditory brainstem: joint coding of interaural level and time differences by the lateral superior olive. In R. Y. Litovsky, M. J. Goupell, R. R. Fay, & A. N. Popper (eds.), *Binaural hearing* (pp. 113–144). Springer, Cham, Switzerland.
- Pangrsic, T., Reisinger, E., & Moser, T. (2012). Otoferlin: A multi-C2 domain protein essential for hearing. *Trends in Neuroscience (Tins)*, **35**, 671–680.
- Parthier, D., Kuner, T., & Körber, C. (2018). The presynaptic scaffolding protein Piccolo organizes the readily releasable pool at the calyx of Held. *Journal of Physiology*, **596**, 1485–1499.
- Petersen, M. B., & Willems, P. J. (2006). Non-syndromic, autosomal-recessive deafness. *Clinical Genetics*, **69**, 371–392.
- Pilati, N., Linley, D. M., Selvaskandan, H., Uchitel, O., Hennig, M. H., Kopp-Scheinflug, C., & Forsythe, I. D. (2016). Acoustic trauma slows AMPA receptor-mediated EPSCs in the auditory brainstem, reducing GluA4 subunit expression as a mechanism to rescue binaural function. *Journal of Physiology*, **594**, 3683–3703.
- Ritzau-Jost, A., Delvendahl, I., Rings, A., Byczkowicz, N., Harada, H., Shigemoto, R., Hirrlinger, J., Eilers, J., & Hallermann, S. (2014). Ultrafast action potentials mediate kilohertz signaling at a central synapse. *Neuron*, **84**, 152–163.
- Rizzoli, S. O., & Betz, W. J. (2005). Synaptic vesicle pools. *Nature Reviews Neuroscience*, **6**, 57–69.
- Rodriguez-Ballesteros, M., Reynoso, R., Olarte, M., Villamar, M., Morera, C., Santarelli, R., Arslan, E., Meda, C., Curet, C., Volter, C., Sainz-Quevedo, M., Castorina, P., Ambrosetti, U., Berrettini, S., Frei, K., Tedin, S., Smith, J., Cruz Tapia, M., Cavalle, L., ... delCastillo, I. (2008). A multicenter study on the prevalence and spectrum of mutations in the otoferlin gene (*OTOF*) in subjects with nonsyndromic hearing impairment and auditory neuropathy. *Human Mutation*, **29**, 823–831.
- Romero, G. E., & Trussell, L. O. (2021). Distinct forms of synaptic plasticity during ascending vs descending control of medial olivocochlear efferent neurons. *Elife*, **10**, e66396.
- Roux, I., Safieddine, S., Nouvian, R., Grati, M., Simmler, M. C., Bahloul, A., Perfettini, I., Le Gall, M., Rostaing, P., Hamard, C., Triller, A., Avan, P., Moser, T., & Petit, C. (2006). Otoferlin, defective in a human deafness form, is essential for exocytosis at the auditory ribbon synapse. *Cell*, **127**, 277–289.
- Sakaba, T., & Neher, E. (2001). Calmodulin mediates rapid recruitment of fast-releasing synaptic vesicles at a calyx-type synapse. *Neuron*, **32**, 1119–1131.
- Sanes, D. H., & Takacs, C. (1993). Activity-dependent refinement of inhibitory connections. *European Journal of Neuroscience*, **5**, 570–574.
- Saviane, C., & Silver, R. A. (2006). Fast vesicle reloading and a large pool sustain high bandwidth transmission at a central synapse. *Nature*, **439**, 983–987.
- Schwaller, B. (2010). Cytosolic Ca²⁺ buffers. *Cold Spring Harbor perspectives in biology*, **2**, a004051.
- Sonntag, M., Englitz, B., Typlt, M., & Rübsamen, R. (2011). The calyx of Held develops adult-like dynamics and reliability by hearing onset in the mouse *in vivo*. *Journal of Neuroscience*, **31**, 6699–6709.
- Starr, A., & Rance, G. (2015). Auditory neuropathy. *Handbook of Clinical Neurology*, **129**, 495–508.
- Sterenborg, J. C., Pilati, N., Sheridan, C. J., Uchitel, O. D., Forsythe, I. D., & Barnes-Davies, M. (2010). Lateral olivocochlear (LOC) neurons of the mouse LSO receive excitatory and inhibitory synaptic inputs with slower kinetics than LSO principal neurons. *Hearing Research*, **270**, 119–126.
- Südhof, T. C. (2004). The synaptic vesicle cycle. *Annual Review of Neuroscience*, **27**, 509–547.
- Sun, J. Y., & Wu, L. G. (2001). Fast kinetics of exocytosis revealed by simultaneous measurements of presynaptic capacitance and postsynaptic currents at a central synapse. *Neuron*, **30**, 171–182.
- Taschenberger, H., & von Gersdorff, H. (2000). Fine-tuning an auditory synapse for speed and fidelity: Developmental changes in presynaptic waveform, EPSC kinetics, and synaptic plasticity. *Journal of Neuroscience*, **20**, 9162–9173.
- Tertrais, M., Bouleau, Y., Emptoz, A., Belleudy, S., Sutton, R. B., Petit, C., Safieddine, S., & Dulon, D. (2019). Viral transfer of mini-otoferlins partially restores the fast component of exocytosis and uncovers ultrafast endocytosis in auditory hair cells of otoferlin knock-out mice. *Journal of Neuroscience*, **39**, 3394–3411.
- Ting, J. T., Daigle, T. L., Chen, Q., & Feng, G. (2014). Acute brain slice methods for adult and aging animals: Application of targeted patch clamp analysis and optogenetics. *Methods in Molecular Biology*, **1183**, 221–242.
- Tritsch, N. X., Rodriguez-Contreras, A., Crins, T. T. H., Wang, H. C., Borst, J. G. G., & Bergles, D. E. (2010). Calcium action potentials in hair cells pattern auditory neuron activity before hearing onset. *Nature Neuroscience*, **13**, 1050–1052.
- Tritsch, N. X., Yi, E., Gale, J. E., Glowatzki, E., & Bergles, D. E. (2007). The origin of spontaneous activity in the developing auditory system. *Nature*, **450**, 50–55.
- Trussell, L. O. (1999). Synaptic mechanisms for coding timing in auditory neurons. *Annual Review of Physiology*, **61**, 477–496.
- Turecek, J., & Regehr, W. G. (2019). Neuronal regulation of fast synaptotagmin isoforms controls the relative contributions of synchronous and asynchronous release. *Neuron*, **101**, 938–949.e4.
- Ulbricht, W. (2005). Sodium channel inactivation: Molecular determinants and modulation. *Physiological Reviews*, **85**, 1271–1301.

- vonGersdorff, H., & Borst, J. G. (2002). Short-term plasticity at the calyx of Held. *Nature Reviews Neuroscience*, **3**, 53–64.
- Walmsley, B., Berntson, A., Leao, R. N., & Fyffe, R. E. (2006). Activity-dependent regulation of synaptic strength and neuronal excitability in central auditory pathways. *Journal of Physiology*, **572**, 313–321.
- Wang, L. Y., & Kaczmarek, L. K. (1998). High-frequency firing helps replenish the readily releasable pool of synaptic vesicles. *Nature*, **394**, 384–388.
- Watanabe, S., & Boucrot, E. (2017). Fast and ultrafast endocytosis. *Current Opinion in Cell Biology*, **47**, 64–71.
- Watanabe, S., Liu, Q., Davis, M. W., Hollopeter, G., Thomas, N., Jorgensen, N. B., & Jorgensen, E. M. (2013). Ultrafast endocytosis at *Caenorhabditis elegans* neuromuscular junctions. *Elife*, **2**, e00723.
- Watanabe, S., Rost, B. R., Camacho-Pérez, M., Davis, M. W., Söhl-Kielczynski, B., Rosenmund, C., & Jorgensen, E. M. (2013). Ultrafast endocytosis at mouse hippocampal synapses. *Nature*, **504**, 242–247.
- Weingarten, D. J. (2018). Maturation of the auditory brainstem after hearing onset: Role of Ca^{2+} sensitivity and vesicle pool organization in reliable synaptic transmission. In *Department of Biology*, pp. 1–87. University of Kaiserslautern, Dissertation.
- Wen, H., Hubbard, J. M., Wang, W. C., & Brehm, P. (2016). Fatigue in rapsyn-deficient zebrafish reflects defective transmitter release. *Journal of Neuroscience*, **36**, 10870–10882.
- Werthat, F., Alexandrova, O., Grothe, B., & Koch, U. (2008). Experience-dependent refinement of the inhibitory axons projecting to the medial superior olive. *Developmental Neurobiology*, **68**, 1454–1462.
- Williges, B., Jürgens, T., Hu, H., & Dietz, M. (2018). Coherent coding of enhanced interaural cues improves sound localization in noise with bilateral cochlear implants. *Trends Hear*, **22**, 1–18.
- Wright, S., Hwang, Y., & Oertel, D. (2014). Synaptic transmission between end bulbs of Held and bushy cells in the cochlear nucleus of mice with a mutation in *otofelin*. *Journal of Neurophysiology*, **34**, 13110–13126.
- Wu, L. G., & Borst, J. G. (1999). The reduced release probability of releasable vesicles during recovery from short-term synaptic depression. *Neuron*, **23**, 821–832.
- Yang, H., & Xu-Friedman, M. A. (2008). Relative roles of different mechanisms of depression at the mouse endbulb of Held. *Journal of Neurophysiology*, **99**, 2510–2521.
- Yang, H., & Xu-Friedman, M. A. (2015). Skipped-stimulus approach reveals that short-term plasticity dominates synaptic strength during ongoing activity. *Journal of Neuroscience*, **35**, 8297–8307.
- Yu, W. M., & Goodrich, L. V. (2014). Morphological and physiological development of auditory synapses. *Hearing Research*, **311**, 3–16.

Additional information

Data availability statement

The data that support the findings of this study are available from the corresponding author upon reasonable request.

Competing interests

None.

Author contributions

All experiments were performed at the University of Kaiserslautern in the Friauf lab. Contribution of each author: NICM: experimental design and project conception, *in vitro* electrophysiology, analysis and interpretation of empirical and modelling data, initial manuscript writing; IP: *in vitro* electrophysiology, analysis of empirical data; LH: *in vitro* electrophysiology, analysis and interpretation of empirical data; JF: analysis and interpretation of empirical and modelling data, manuscript writing; AS: computational modelling; EF: experimental design and project conception, interpretation of empirical and modelling data, manuscript writing. All authors edited the manuscript and have approved its final version.

Funding

This study was funded by German Research Foundation (DFG) grant FR1784/21–1 to EF, BMBF/NIDCD grant 01GQ2001 (ModSynTrans) to EF, and NIH/NIDCD grant R01DC019268-01 to AS.

Acknowledgements

The authors thank R Reiss, K Ociepa and J Winkelhoff for excellent technical assistance. Finally, the authors also thank Dr Elisa Krächan and Dr Erika Pizzi for helpful comments on an early and a late version of the manuscript, respectively.

Open Access funding enabled and organized by Projekt DEAL.

Author's present address

I. Paulußen: Department of Neurosurgery, University of Bonn Medical Centre, Bonn, D-53127 Germany

Keywords

action potential fidelity, circuit maturation, deafness, hearing experience, *otofelin*, replenishment of synaptic vesicles, synaptic attenuation, synaptic strength, synaptic transmission

Supporting information

Additional supporting information can be found online in the Supporting Information section at the end of the HTML view of the article. Supporting information files available:

Statistical Summary Document

Peer Review History

Supporting Information for online publication (Data set/Video/Audio only)